ALMA-IMF. XIV. Free–Free Templates Derived from H41α and Ionized Gas Content in 15 Massive Protoclusters

Roberto Galván-Madrid, Daniel Díaz-González, Frédérique Motte, Adam Ginsburg, Nichol Cunningham, Karl Menten, Mélanie Armante, Mélisse Bonfand, Jonathan Braine, Timea Csengeri, et al.

The Astrophysical Journal Supplement Series, 274:15 (23pp), 2024 September https://doi.org/10.3847/1538-4365/ad61e6

ALMA-IMF. XIV. Free–Free Templates Derived from H41α and Ionized Gas Content in 15 Massive Protoclusters

Roberto Galván-Madrid[1], Daniel J. Díaz-González[1], Frédérique Motte[2], Adam Ginsburg[3], Nichol Cunningham[2,4], Karl M. Menten[5], Mélanie Armante[6,7], Mélisse Bonfand[8], Jonathan Braine[9], Timea Csengeri[9], Pierre Dell'Ova[6,7], Fabien Louvet[2], Thomas Nony[1,10], Rudy Rivera-Soto[1], Patricio Sanhueza[11,12], Amelia M. Stutz[13], Friedrich Wyrowski[5], Rodrigo H. Álvarez-Gutiérrez[13], Tapas Baug[14], Sylvain Bontemps[9], Leonardo Bronfman[15], Manuel Fernández-López[16], Antoine Gusdorf[6,7], Atanu Koley[13], Hong-Li Liu[17], Javiera Salinas[13], Allison P. M. Towner[18], and Anthony P. Whitworth[19]
[1] Instituto de Radioastronomía y Astrofísica, Universidad Nacional Autónoma de México, Morelia, Michoacán 58089, Mexico; r.galvan@irya.unam.mx
[2] Univ. Grenoble Alpes, CNRS, IPAG, 38000 Grenoble, France
[3] Department of Astronomy, University of Florida, PO Box 112055, USA
[4] SKA Observatory, Jodrell Bank, Lower Withington, Macclesfield SK11 9FT, UK
[5] Max-Planck-Institut für Radioastronomie, Auf dem Hügel 69, 53-121 Bonn, Germany
[6] Laboratoire de Physique de l'École Normale Supérieure, ENS, Université PSL, CNRS, Sorbonne Université, Université de Paris, 75005 Paris, France
[7] Observatoire de Paris, PSL University, Sorbonne Université, LERMA, 75014 Paris, France
[8] Departments of Astronomy and Chemistry, University of Virginia, Charlottesville, VA 22904, USA
[9] Laboratoire d'astrophysique de Bordeaux, Univ. Bordeaux, CNRS, B18N, allée Geoffroy Saint-Hilaire, 33615 Pessac, France
[10] INAF—Osservatorio Astrofisico di Arcetri, Largo E. Fermi 5, 50125 Firenze, Italy
[11] National Astronomical Observatory of Japan, National Institutes of Natural Sciences, 2-21-1 Osawa, Mitaka, Tokyo 181-8588, Japan
[12] Department of Astronomical Science, SOKENDAI (The Graduate University for Advanced Studies), 2-21-1 Osawa, Mitaka, Tokyo 181-8588, Japan
[13] Departamento de Astronomía, Universidad de Concepción, Casilla 160-C, 4030000 Concepción, Chile
[14] S. N. Bose National Centre for Basic Sciences, Sector-III, Salt Lake, Kolkata 700106, India
[15] Departamento de Astronomía, Universidad de Chile, Las Condes, 7591245 Santiago, Chile
[16] Instituto Argentino de Radioastronomía (CCT-La Plata, CONICET; CICPBA), C.C. No. 5, 1894, Villa Elisa, Buenos Aires, Argentina
[17] School of Physics and Astronomy, Yunnan University, Kunming, 650091, People's Republic of China
[18] University of Arizona Department of Astronomy and Steward Observatory, 933 North Cherry Avenue, Tucson, AZ 85721, USA
[19] School of Physics and Astronomy, Cardiff University, Cardiff CF24 3AA, UK
Received 2024 February 20; revised 2024 June 15; accepted 2024 June 28; published 2024 September 4

Abstract

We use the H41α recombination line to create templates of the millimeter free–free emission in the ALMA-IMF continuum maps, which allows us to separate it from dust emission. This method complements spectral-index information and extrapolation from centimeter-wavelength maps. We use the derived maps to estimate the properties of up to 34 H II regions across the ALMA-IMF protoclusters. The hydrogen ionizing photon rate Q_0 and spectral types follow the evolutionary trend proposed by Motte et al. The youngest protoclusters lack detectable ionized gas, followed by protoclusters with increasing numbers of OB stars. The total Q_0 increases from $\sim 10^{45}$ s^{-1} to $>10^{49}$ s^{-1}. We used the adjacent He41α line to measure the relative number abundances of helium, finding values consistent with the Galactic interstellar medium, although a few outliers are discussed. A search for sites of maser amplification of the H41α line returned negative results. We looked for possible correlations between the electron densities, emission measures, and Q_0 with H II region size D. The latter is the best correlated, with $Q_0 \propto D^{2.49 \pm 0.18}$. This favors interpretations in which smaller ultracompact H II regions are not necessarily the less dynamically evolved versions of larger ones but rather are ionized by less massive stars. Moderate correlations were found between the dynamical width $\Delta V_{\rm dyn}$ with D and Q_0. $\Delta V_{\rm dyn}$ increases from about 1 to 2 times the ionized-gas sound speed. Finally, an outlier H II region south of W43-MM2 is discussed. We suggest that this source could harbor an embedded stellar or disk wind.

Unified Astronomy Thesaurus concepts: H II regions (694); Star forming regions (1565); Millimeter astronomy (1061)

1. Introduction

The ALMA-IMF Large Program targeted 15 of the most massive star-forming clumps within 5 kpc from the Sun (Csengeri et al. 2017), based on the larger ATLASGAL sample across the Galaxy (Schuller et al. 2009; Csengeri et al. 2014). The survey description has been presented in Motte et al. (2022), including a proposed evolutionary scheme for the sample based on their activity in the mid- and far-infrared, as well as the presence of hydrogen recombination line emission. The ALMA-IMF consortium has provided science-ready data products to the community, including 12 m array continuum images, together with an imaging and self-calibration pipeline (Ginsburg et al. 2022b), a combination with single-dish bolometer images (Díaz-González et al. 2023), and full-bandwidth line cubes (Cunningham et al. 2023). The two-band (3 mm and 1 mm), two-configuration, mosaic observing mode allows us to map the extent of these protocluster clumps with excellent imaging quality (Ginsburg et al. 2022b).

The main scientific driver of the project is to measure the core mass function (CMF) in a statistically significant (>500)

sample of cores that spans the full range of gas masses, from subsolar to $\gtrsim$100 $M_\odot$ (e.g., Motte et al. 2018), something that can only be achieved by observing massive protocluster clumps at different evolutionary stages. The more evolved protocluster clumps in the sample have increasingly important feedback by ionization from ultracompact (UC) and hypercompact (HC) H II regions (e.g., Kurtz et al. 1994; Churchwell 2002; Hoare et al. 2007; Purcell et al. 2013; Klaassen et al. 2018). The corresponding free–free continuum emission can be an important "contaminant" for the otherwise dust-only Atacama Large Millimeter/submillimeter Array (ALMA) millimeter continuum maps. The separation of dust and free–free contributions is therefore a necessary step for the correct interpretation of the origin of the emission and derived quantities (e.g., Galván-Madrid et al. 2009; Zhang et al. 2022). The first results on the evolution of the CMF in young protoclusters mostly devoid of H II regions were presented in Pouteau et al. (2022, 2023) and Nony et al. (2023). The CMF of the evolved protocluster G012.80 is presented in Armante et al. (2024), who used the results presented in this paper. The CMFs of the global sample, and also as a function of the evolution class, are reported in Louvet et al. (2024).

ALMA-IMF has been designed to include tools to separate the free–free contribution. The first one is the use of spectral index information (Pouteau et al. 2022; Nony et al. 2023; Díaz-González et al. 2023). However, it is desirable to have an alternative marker that also provides an estimation of the free–free contribution in intensity units, i.e., as a map. Recombination lines are useful tools to detect and characterize the H II regions produced by massive star and cluster formation (e.g., Rugel et al. 2019; Anderson et al. 2021). Lines in the (sub) millimeter are brighter than their centimeter counterparts and mostly free from collisional ("pressure") broadening; thus they are useful to characterize the denser H II regions (e.g., Keto et al. 2008; Nguyen-Luong et al. 2017; Kim et al. 2017). Moreover, their brightness has been shown to be globally consistent with local thermodynamic equilibrium (LTE) in massive star formation regions (Kim et al. 2018). Therefore, the velocity-integrated line intensity can be used to estimate the underlying free–free continuum (e.g., Liu et al. 2019). This method offers several advantages, namely: covering the whole survey, having approximately the same UV coverage and beam size as the corresponding continuum images, and providing the estimate of the free–free contribution directly at a similar frequency to the continuum. The latter decreases the potential effect of assuming a wrong free–free spectral index, as could be the case if extrapolation from centimeter-wavelength data is employed. However, the method is not without its caveats, mainly that the line can be out of LTE under certain conditions (e.g., Walmsley 1990; Peters et al. 2012), and molecular-line contamination.

In this paper, we propose to use the H41α line data within the same ALMA-IMF data set. In Section 2 we describe the data. In Section 3 we explain the procedure to obtain the free–free estimation and error maps, the products that we make available, and a validation of the procedure and its limitations. In Section 4 we derive the physical properties for the H II regions in the ALMA-IMF protoclusters. In Section 5 we use the H41a and He41α line parameters to derive relative He abundances in the ionized gas. In Section 6 we discuss the benefits and caveats of our proposed technique, look for candidates of recombination line masers, and further discuss the evolution of photoionization within the ALMA-IMF sample.

2. Data

For each of the 15 ALMA-IMF protoclusters, we created cubes that cover the 41α recombination lines of hydrogen (H41α), helium (He41α), and carbon (C41α). The rest frequencies of the targeted lines are, respectively, 92.034434, 92.071938, and 92.080355 GHz, which correspond to velocity offsets of the He and C lines with respect to H41α of -122.165 and -149.583 km s^{-1}. All the cubes were made covering a total width of 270 km s^{-1}. The reference velocities for the cube construction were set to the LSR systemic velocities of each protocluster reported in Table 1 of Motte et al. (2022). The cubes were created in `CASA` version 6.3.0 (CASA Team et al. 2022) using the ALMA-IMF data pipeline (Ginsburg et al. 2022b). We followed the procedures developed for the imaging of cubes as described in Cunningham et al. (2023).

Each cube is cleaned down to a residual level of $\times$3 to $\times$5 the rms noise ($\sigma_{\rm rms}$) of channels with H41α emission. This is defined using the `threshold` parameter of the `tclean` task. Also, `startmodel` is used based on the continuum images published in Ginsburg et al. (2022b). This permits `tclean` to run significantly faster because the Fourier transform of `startmodel` is subtracted from the visibilities at the beginning of the cleaning process (see Cunningham et al. 2023). Multiscale cleaning is used by setting the `deconvolver` and `scales` parameters in `tclean`. The scales are selected to clean model components of size zero (point source), the beam size, and multiples of $\times$2 the beam size until reaching $\sim$8″, or about half of the largest recoverable scale in the data (Díaz-González et al. 2023). The `gain` parameter was set to 0.08 for all the cubes, which is slightly slower than the default (0.1) in `CASA`. This can be afforded in the case of line-specific cubes. Finally, the JvM correction (Jorsater & van Moorsel 1995) is applied to the `CASA`-generated cubes in order to correct the flux scale of the residuals and of the restored image due to the fact that the volumes of the clean and dirty beams are not equal.[20] The cleaning parameters are available in the `imaging_parameters.py` script in the public repository of the ALMA-IMF data-processing pipeline.[21]

3. Free–Free Estimations

3.1. Procedure

We use the H41α line to create maps of the free–free emission at the frequencies of the ALMA-IMF continuum images in Bands 3 and 6. Using a recombination line within the ALMA-IMF data sets ensures to have a similar (u, v) coverage and angular resolution as the continuum images.

The free–free estimations are useful to the main scientific case of the ALMA-IMF project of characterizing the dust emission of the dense-core population in the target protoclusters. For this science case, the free–free component is mainly considered as a contaminant of the dust continuum emission, but it can also be used to estimate the properties of

[20] The scripts to apply the JvM correction that were used for the imaging presented in this paper and in Cunningham et al. (2023) can be found in https://github.com/radio-astro-tools/beam-volume-tools.
[21] https://github.com/ALMA-IMF/reduction

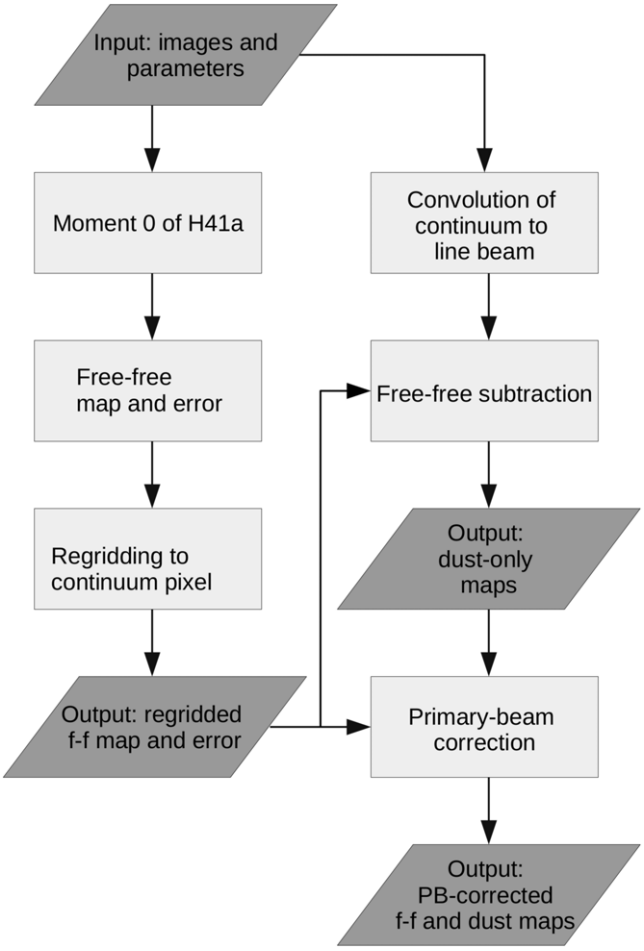

Figure 1. Flowchart of the procedure to create two types of output in each of the observed ALMA continuum bands: free–free maps with their associated errors, and estimation maps of dust-only emission. The primary-beam-corrected versions of the previous two are calculated at the end of the procedure.

the H II regions produced by the young (∼zero-age main sequence, ZAMS) stellar population.

Figure 1 summarizes the procedure that we execute for each protocluster and band. First, three input images for a given protocluster are read in: the H41α line cube and one continuum image for each band. Then, a velocity-integrated intensity (moment 0) map $\sum I_{\rm H41}\,\Delta$v in units of Jy beam^{-1} km s^{-1} is created for each field. The velocity range is optimized by visual inspection to cover only channels where the line is detected. A default value of ± 10 km s^{-1} from the cloud systemic velocity is used for the protoclusters where the line is faint or nondetected (see below). After this, the free–free estimation map $I_{\rm ff}$ in units of Jy beam^{-1} is constructed using the following equation (e.g., Wilson et al. 2009; Wenger et al. 2019):

$$I_{\rm ff} = 1.432 \times 10^{-4} (\nu_0^{-1.1}\, T_e^{1.15})(1 + N_{\rm He}/N_{\rm H}) \sum I_{\rm H41}\,\Delta v, \quad (1)$$

where the electron temperature is $T_e = 7000$ K, the helium-to-hydrogen number ratio is $N_{\rm He}/N_{\rm H} = 0.08$, and ν_0 is the central frequency of the H41α line. Equation (1) assumes LTE conditions, and we found a posteriori that this assumption is generally valid (see Section 6.2). T_e in H II regions is expected to have values from $\gtrsim$5000 K to $\approx 10^4$ K (Osterbrock 1989). Our selection is close to the middle of this range and minimized regions of oversubtraction of the free–free emission in the continuum maps. The selected value of $N_{\rm He}/N_{\rm H}$ is appropriate for the Milky Way interstellar medium (ISM; Méndez-Delgado et al. 2020), and later we show that the H II regions in our sample are mostly consistent with it (see Section 5). Further updates in $N_{\rm He}/N_{\rm H}$ only change $I_{\rm ff}$ by a few percent (see Equation (1)). We consider a 20% error in T_e and propagate it through our measurements to acknowledge the possibility of spatial variations in this quantity. In many of the derived quantities, this uncertainty dominates the errors.

At millimeter wavelengths, it is expected that free–free emission will be optically thin (spectral index $\alpha_{\rm ff} = -0.1$) in all H II regions except possibly in the densest ones (e.g., Keto 2002; Galván-Madrid et al. 2009; Rosero et al. 2019). The actual detection of H41α guarantees that the underlying free–free continuum is not opaque; otherwise, the line would be absorbed. For a homogeneous H II region, the transition or turnover frequency between the optically thick and thin regimes is in the range from 50 GHz to 60 GHz for an emission measure (EM; see Section 4) as high as 10^{10} cm^{-6} pc (Kurtz 2005), although H II regions with density gradients could be partially optically thick ($\alpha_{\rm ff} \sim 1$) at frequencies $\gtrsim$100 GHz (Keto et al. 2008; Galván-Madrid et al. 2009). In our procedure, the output free–free map at the frequency of H41α (92.03 GHz) is rescaled to the desired frequency of the continuum image assuming $\alpha_{\rm ff} = -0.1$. The flux scalings to the Band 3 (98.6 GHz) and Band 6 (224.6 GHz) continuum frequencies are then 0.99 and 0.92, respectively. If the correct free–free spectral index in those spots were $\alpha = 1$ all the way to Band 6, the continuum scaling factors should instead be 1.07 and 2.44. It is possible that in Band 3 the optically thin assumption breaks in a few compact spots with very dense H II regions, but this is highly unlikely in Band 6.

Maps of the error of the free–free intensity $\sigma_{\rm ff}$ are also generated. These are approximated by the noise in the moment 0 map $\sigma_{\rm m0}$ and the error in the assumed electron temperature σ_{T_e} as in

$$\sigma_{\rm ff} \approx I_{\rm ff} \left[\left(\frac{\sigma_{\rm m0}}{\sum I_{\rm H41}\,\Delta v} \right)^2 + \left(\frac{\sigma_{T_e}}{T_e} \right)^2 \right]^{0.5}. \quad (2)$$

The $I_{\rm ff}$ and $\sigma_{\rm ff}$ maps are regridded to the pixel geometry of the input continuum images, which in turn are convolved to the slightly larger beam size (see Cunningham et al. 2023) of the line cube and moment 0 maps. A subtraction is then performed of the convolved continuum image minus the regridded free–free map, resulting in an estimated map of pure-dust emission $I_{\rm dust}$. Finally, primary-beam (PB) correction is applied to the regridded free–free estimation map and the associated error map, as well as to the pure-dust map. Performing the PB correction as a last step has the advantage of working with images with spatially uniform noise levels in the intermediate steps.

3.2. Products

Figure 2 shows the PB-corrected free–free estimation maps for the 12 ALMA-IMF protoclusters with detection of H41α emission. Figure 10 in Appendix A gives a comparison between the original continuum maps, the free–free estimations, and the pure-dust maps at 1.3 mm.

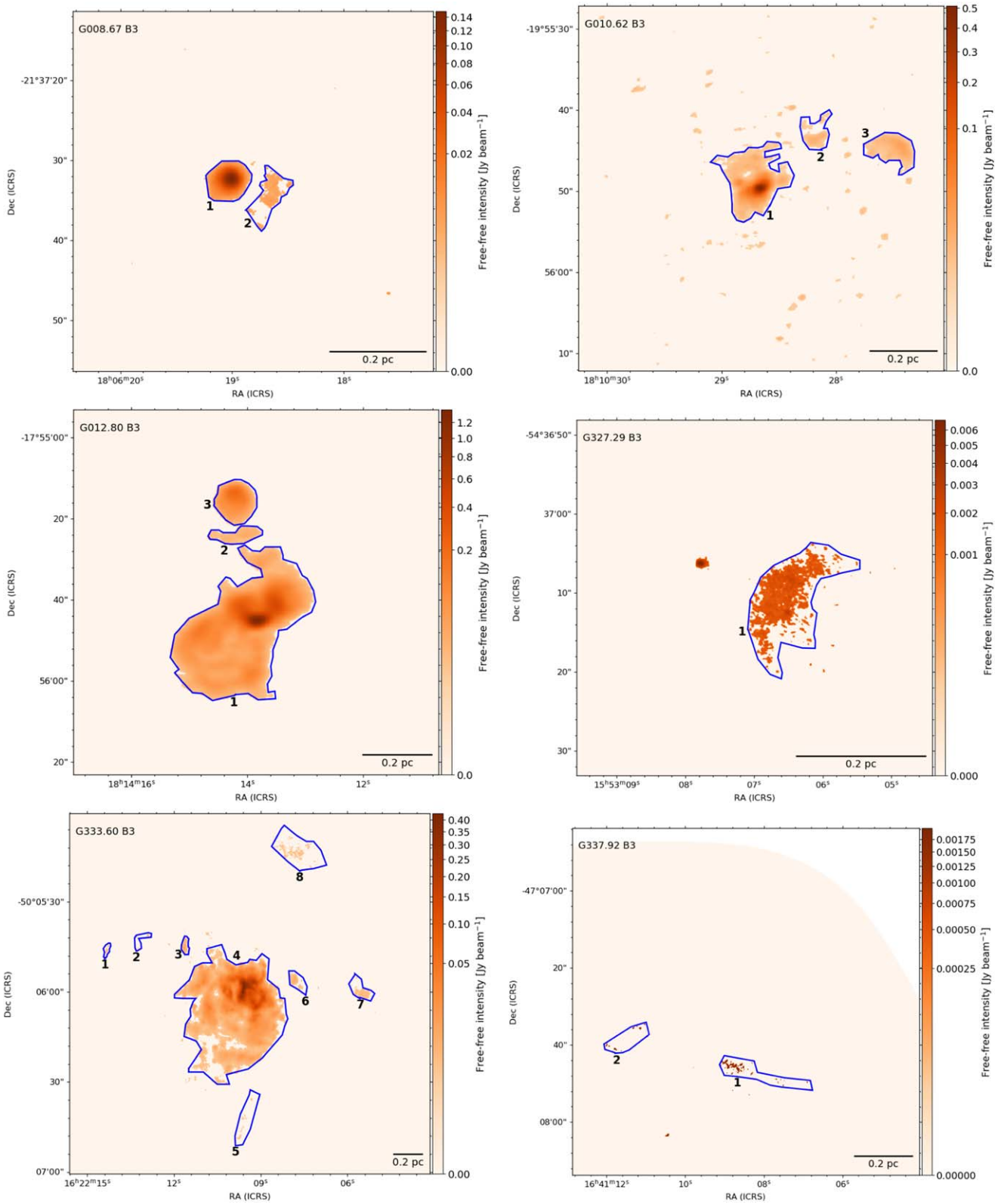

Figure 2. Free–free estimation maps in Band 3 for protoclusters G008.67 (top left), G010.62 (top right), G012.80 (second left), G327.29 (second right), G333.60 (third left), G337.92 (third right), G351.77 (fourth left), G353.41 (fourth right), W43-MM2 (fifth left), W43-MM3 (fifth right), W51-E (bottom left), and W51-IRS2 (bottom right). The compact emission at the center of G327.29 is dominated by contamination from molecular lines (see Section 3.3).

The free–free estimation is only performed in pixels of the moment 0 maps above a threshold of 5σ, where σ is defined as the robust standard deviation using the median absolute deviation (MAD) implemented in `astropy.stats.mad_std`. Table 1 lists the basic parameters for the preparation of the free–free estimation images. Two protoclusters were clear nondetections in H41α (G338.93 and W43-MM1). One protocluster (G328.25) was a tentative detection, but further

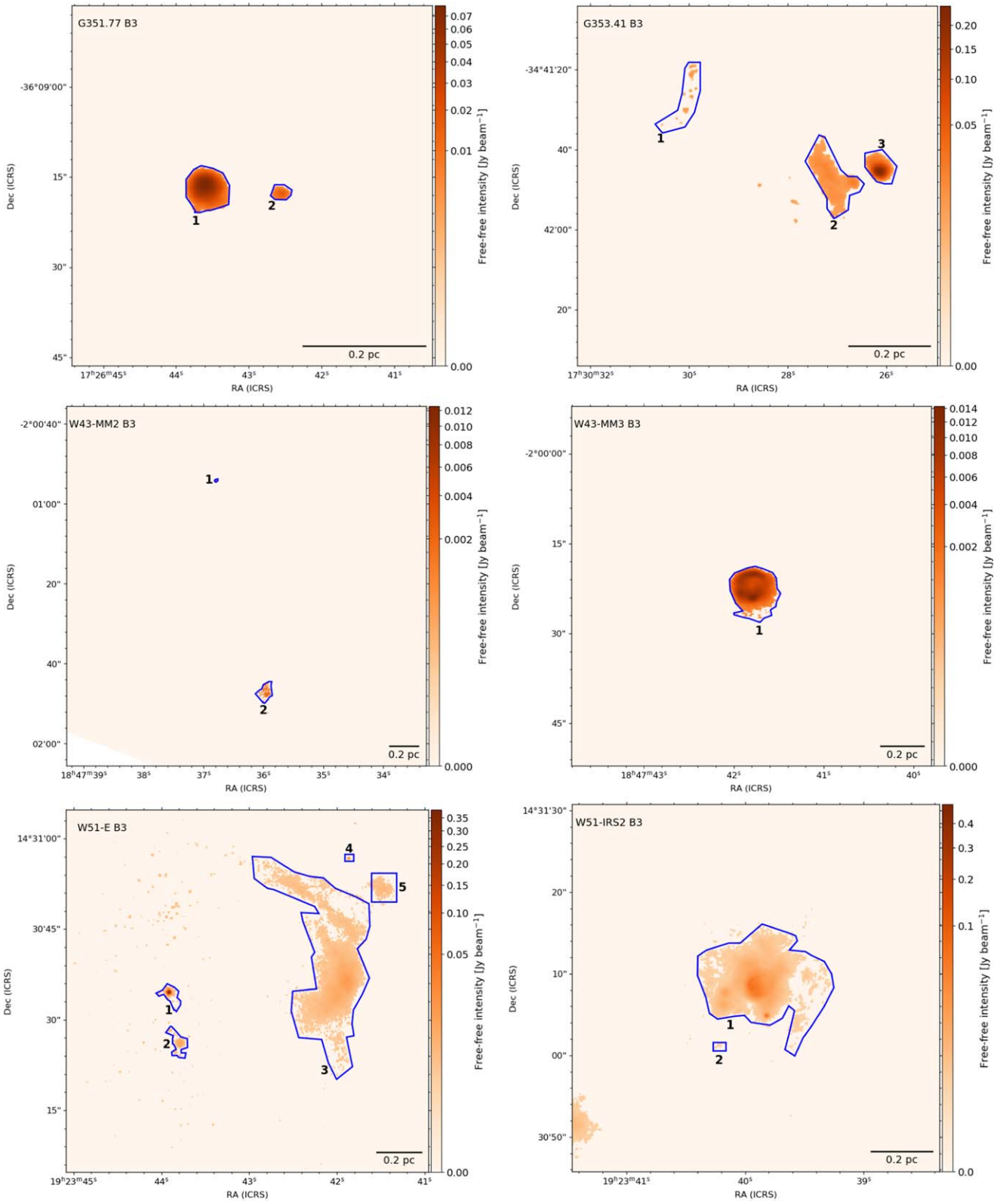

Figure 2. (Continued.)

inspection showed the spectrum was dominated by molecular-line contamination. The free–free estimation maps of these three protoclusters originally contained a few pixels with values larger than zero due to molecular lines in the moment 0 integration; therefore, we manually set their free–free maps to zero.

The data products are further described in Appendix B. The scripts associated with this paper[22] permit the user to easily recalculate any free–free estimation image by editing

[22] https://github.com/ALMA-IMF/h41a-freefree

Table 1
H41α Cube and Moment 0 Parameters

Protocluster	HPBW, PA (arcsec × arcsec, deg)	(v_{min}, v_{max}) (km s^{-1})	σ_{m0} (mJy beam^{-1} km s^{-1})
G008.67	0.95 × 0.66, 66.7	[6.8, 84.0]	20
G010.62	0.57 × 0.45, −67.9	[−39.1, 41.9]	14
G012.80	2.28 × 1.93, 84.9	[−5.8, 84.4]	83
G327.29	0.71 × 0.61, 57.2	[−63.4, −19.2]	9
G328.25†	0.99 × 0.93, 75.0	[−53.0, −33.0]	9
G333.60	0.78 × 0.74, 28.2	[−103.3, 5.2]	19
G337.92	0.80 × 0.75, −77.5	[−52.8, −8.7]	9
G338.93†	0.66 × 0.63, 4.7	[−72.0, −52.0]	5
G351.77	2.20 × 1.90, 89.8	[−29.0, 20.6]	42
G353.41	2.18 × 1.85, 73.6	[−46.7, 19.5]	55
W43-MM1†	0.92 × 0.52, −81.9	[80.3, 115.3]	6
W43-MM2	0.43 × 0.33, −77.8	[61.9, 122.6]	5
W43-MM3	0.61 × 0.43, −84.0	[61.1, 120.0]	7
W51-E	0.39 × 0.35, −73.0	[22.8, 100.0]	11
W51-IRS2	0.41 × 0.37, −68.8	[8.7, 93.4]	11

Note. Columns: (1) protocluster name; (2) cube half-power beamwidth and position angle; (3) visually determined velocity range of the moment 0 integration (a default ±10 km s^{-1} is used for the nondetections marked with a †); (4) MAD standard deviation of the moment 0 image.

`ffsub.py`, which makes use of the functions defined in `ff_tools.py`. The code can also be easily applicable to other data sets (e.g., Nony et al. 2024, for ALMA observations of the W49N protocluster with observations of H30α). We caution the user against blindly using the calculated free–free templates in regions where it dominates the total continuum emission, or at the position of line-rich hot molecular cores. In the former case, the generated error maps (σ_{ff}) become particularly useful to weigh in the relative contributions of dust and free–free. In the latter, molecular lines can dominate over the recombination line emission.

3.3. Validation

A typical method to separate the contributions of dust and free–free in (sub)millimeter continuum maps is to use a centimeter continuum map dominated by free–free and extrapolate it to shorter wavelengths, assuming an appropriate spectral index (e.g., Carrasco-González et al. 2012; Zhang et al. 2022). However, for a survey such as ALMA-IMF, using the H41α line within the same data set has several advantages, namely: (i) that the assumed $\alpha_{ff} = -0.1$ is more likely to be correct when the scaling is done within millimeter wavelengths, and not from the centimeter to the millimeter, also, the scaling is smaller; (ii) that the (u, v) coverages of the continuum and line maps are very similar and thus their beam sizes and largest recoverable scales are also quite similar; (iii) that there are no extra induced flux-calibration or astrometric errors from using different instruments; and (iv) that 10 out of 15 ALMA-IMF protoclusters have declinations $< -15°$, which makes them difficult to observe with the Very Large Array (VLA), at least with a good synthesized beam.[23] Actually, 5 out of 10 protoclusters are unobservable with the VLA.

To cross-validate our method, we compare the H41α-derived free–free estimation $I_{ff,H41}$ at 98 GHz for the W51 protoclusters to an independent estimation $I_{ff,2cm}$ derived from the Ku-band (2.2 cm, 13.4 GHz) VLA image presented in Ginsburg et al. (2016). The beam size and position angle of the original 2 cm image are BMAJ = 0.″342, BMIN = 0.″332, and BPA = 14.83 deg. We convolve this image to the beam of the H41α-derived free–free map: BMAJ = 0.″408, BMIN = 0.″374, and BPA = −68.77 deg, and regrid it to the same pixel geometry. Next, we assume that the 2 cm free–free emission is optically thin and rescale the centimeter map by a factor of $(98.6/13.4)^{-0.1}$ to estimate the free–free intensity in the ALMA-B3 map. Finally, we mask out all pixels below $5\sigma = 5 \times 92$ μJy beam^{-1}, where σ is defined as in Section 3.2.

Figure 3 shows a comparison of the free–free maps at 98.6 GHz derived using the H41α line and the 2 cm continuum. The comparison is done for those pixels with a valid measurement (i.e., $>5\sigma$) in both images. It is seen that the vast majority of pixels follow the line where the ratio of the estimations $I_{ff,H41}/I_{ff,2cm} = 1$. From 145,862 pixels in the left panel of Figure 3, 96.8% are within 3σ of the one-to-one relation, where σ is determined for each pixel using the H41α free–free error map. The outlier pixels can be separated into two categories, bright and faint. The bright outliers (red points), those pixels with $I_{ff,H41} > 0.025$ Jy beam^{-1} and beyond 3σ from $I_{ff,H41}/I_{ff,2cm} = 1$, are only 328 pixels, or 4.7 times the beam area. Further inspection reveals that these pixels are located exactly at the position of the two well-known UC H II regions: d2 in W51-IRS2 and e2 W51-E (e.g., Zhang et al. 1998; Goddi et al. 2016).

Figure 4 shows the two previously mentioned regions overlaid on the integrated emission of CH_3CN in Band 3. The red contours mark the location of the bright outliers (central panel of Figure 3). In the literature, the e2 region (top row of Figure 4) is subdivided into the bright UC H II region e2-west (e2w) and the hot-core emission peaks e2e and e2nw (e.g., Shi et al. 2010; Ginsburg et al. 2017). The bright-outlier region matches mostly with e2w. The underlying continuum of this H II region is bright enough to absorb the CH_3CN line. The recombination line spectrum within this mask (top right panel of Figure 4) shows a clear detection of the H41α and He41α lines, without evidence of significant contamination from molecular lines. The bottom row of Figure 4 shows the second region with bright outliers, which matches the position of the

[23] In the ancillary VLA continuum data for the observable ALMA-IMF protoclusters, the synthesized beam is usually larger and always more elliptical than in the ALMA images (R. Rivera-Soto et al. 2024, in preparation).

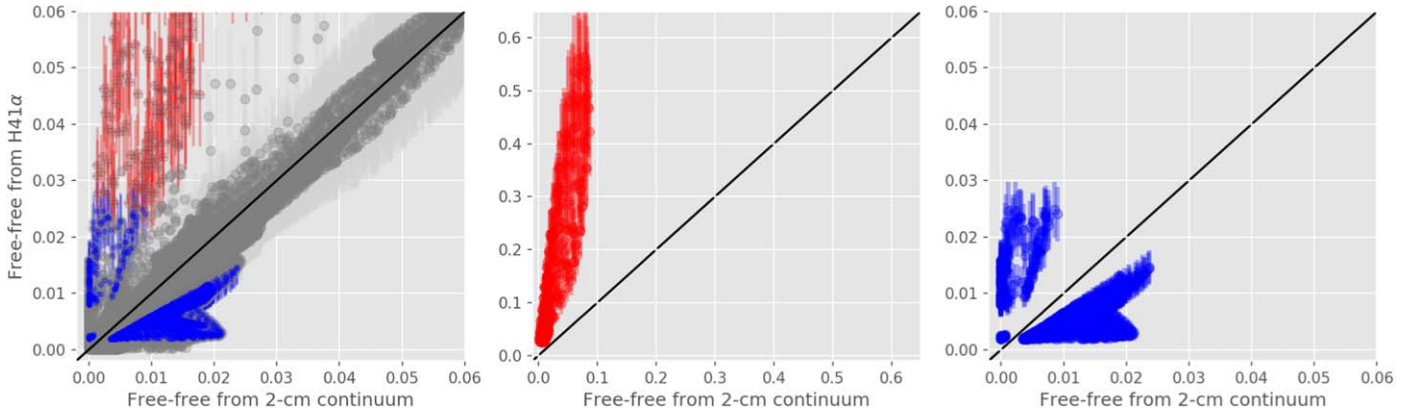

Figure 3. Validation of the procedure to estimate the free–free emission in the ALMA-IMF maps via the H41α line. The plots show a pixel-by-pixel comparison between the free–free intensity at 3 mm derived from H41α vs. that derived from the 2 cm continuum, assuming a spectral index of −0.1. We used the W51-IRS2 and W51-E protoclusters, for which there are also high-quality VLA data at a similar angular resolution (Ginsburg et al. 2016). The left panel shows all the 145,862 pixels with an intensity above 5σ in both maps. 96.8% of those pixels fall within ±3σ of the one-to-one relation. The middle panel shows the 0.2% of the pixels that are defined as bright outliers; their location is analyzed in Figure 4. The right panel shows the faint outliers (3% of the pixels), which are mostly in the periphery of H II regions and have a lower signal-to-noise ratio. The colored points and bars in the middle and right panels have the same color as their error bars in the left panel.

UC H II region W51 d2. The situation is very similar to that of e2, except that the background continuum is not bright enough to produce absorption of the CH_3CN line.

From the previous analysis, we conclude that the origin of the H41α bright-outlier areas could either be: (i) a true yet moderate enhancement of the recombination line compared to LTE conditions; or (ii) the optically thin free–free extrapolation from 13 GHz to 98 GHz being invalid, i.e., having partially optically thick free–free emission with a spectral index $-0.1 < \alpha_{\rm ff} < 2$; or a combination of the two. For the case of W51, the spots of bright-outlier H41α emission do not appear to have significant contamination from molecular lines (in W51-E and W51-IRS2 we integrated the velocity ranges [22.8,100] and [8.7,93.4] km s^{-1}, respectively; see Table 1). We have inspected the correspondence of the 76 sources in the hot molecular core (HMC) catalog of Bonfand et al. (2024) with our recombination line maps. Eighteen HMCs overlap with valid pixels in our free–free estimation maps. Analysis of the spectra around their positions shows that recombination line emission dominates in all cases except for G327 HMC 1 and G337 HMCs 1 and 4. These areas are not labeled as H II regions in Figure 2 and are therefore excluded from our analysis.

4. H II Region Properties

We use the derived 3 mm free–free maps to estimate the average properties of H II regions in the ALMA-IMF protoclusters. For this, we first define the apertures of distinct H II emission in each of the 12 protoclusters with recombination line detection (see Section 3.2). The apertures are marked in Figure 2 and provided in the data release (`.reg` files) associated with this paper. We then used the following equations (see, e.g., Wilson et al. 2009; Rivera-Soto et al. 2020) to derive their average EMs (pc cm^{-6}), electron densities (n_e, cm^{-3}), and hydrogen-ionizing photon rates (Q_0, s^{-1}):

$$\tau_{\rm ff} = \ln\left[\left(1 - \frac{I_\nu}{B_\nu(T_e)}\right)^{-1}\right], \quad (3)$$

$$\mathrm{EM} = 12.143\tau_{\rm ff}\left[\frac{\nu}{\mathrm{GHz}}\right]^{2.1}\left[\frac{T_e}{\mathrm{K}}\right]^{1.35} = \int n_e^2\, dl, \quad (4)$$

$$Q_0 = \frac{\pi}{6}\alpha_{\rm B} n_e^2 D^3 = \frac{\pi}{6}\alpha_{\rm B} D^2 \mathrm{EM}, \quad (5)$$

where $\tau_{\rm ff}$ is the free–free continuum optical depth, I_ν is the average intensity of the pixels within the aperture, $B_\nu(T_e)$ is the Planck function at the electron temperature T_e, and $\alpha_{\rm B} = 2\times10^{-13}$ cm^3 s^{-1} is the case-B hydrogen recombination coefficient. The optical depth $\tau_{\rm ff}$ is almost a direct observable that depends only on the intensity and the assumed T_e. However, in Equations (4) and (5) the EM, Q_0, and n_e are not independent quantities. By definition, EM is integrated into the line of sight across the ionized object; thus under spherical geometry the diameter of the emitting H II region is $\int dl = D$. In practice, EM is calculated first from $\tau_{\rm ff}$ using Equation (4), and then n_e and Q_0 are calculated using Equations (4) and (5). Our spherical approximation will be good for H II regions that are isolated and round. For example, for the central H II region in G010.6, from 3D radiative transfer modeling of the H30α line, the inferred Q_0 is 6 to 7×10^{48} s^{-1} (Galván-Madrid et al. 2023), which is consistent with the spherical value reported here: $5.1\pm1.4\times10^{48}$ s^{-1}.

Table 2 lists the average physical parameters derived for the H II regions in the ALMA-IMF protoclusters, ordered by the sum of the Q_0 of the H II regions in each protocluster. The spectral types of the ionizing stars are determined using the calibrations of Martins et al. (2005) for O-type stars and of Panagia (1973) for B-type stars. A single ionizing star is assumed. For reference, Table 2 also lists the evolutionary stage (young, intermediate, or evolved) of the ALMA-IMF protoclusters determined by Motte et al. (2022) from a combination of mid- and far-infrared emission, and also considering the H41α surface brightness in preliminary cubes. Our measurements of the ionized gas are overall consistent with this classification, both in terms of EM and Q_0. The earliest spectral type and amount of OB stars in each protocluster is also consistent with the proposed evolutionary picture: the youngest regions are devoid of massive stars, followed by regions with a few B-type stars, and then the most active protoclusters harbor a few to several massive stars, including O-type stars. However, a few sources deserve a special mention. The ALMA-IMF mosaics of W43-MM2 also cover the region known as MM13 (Motte et al.

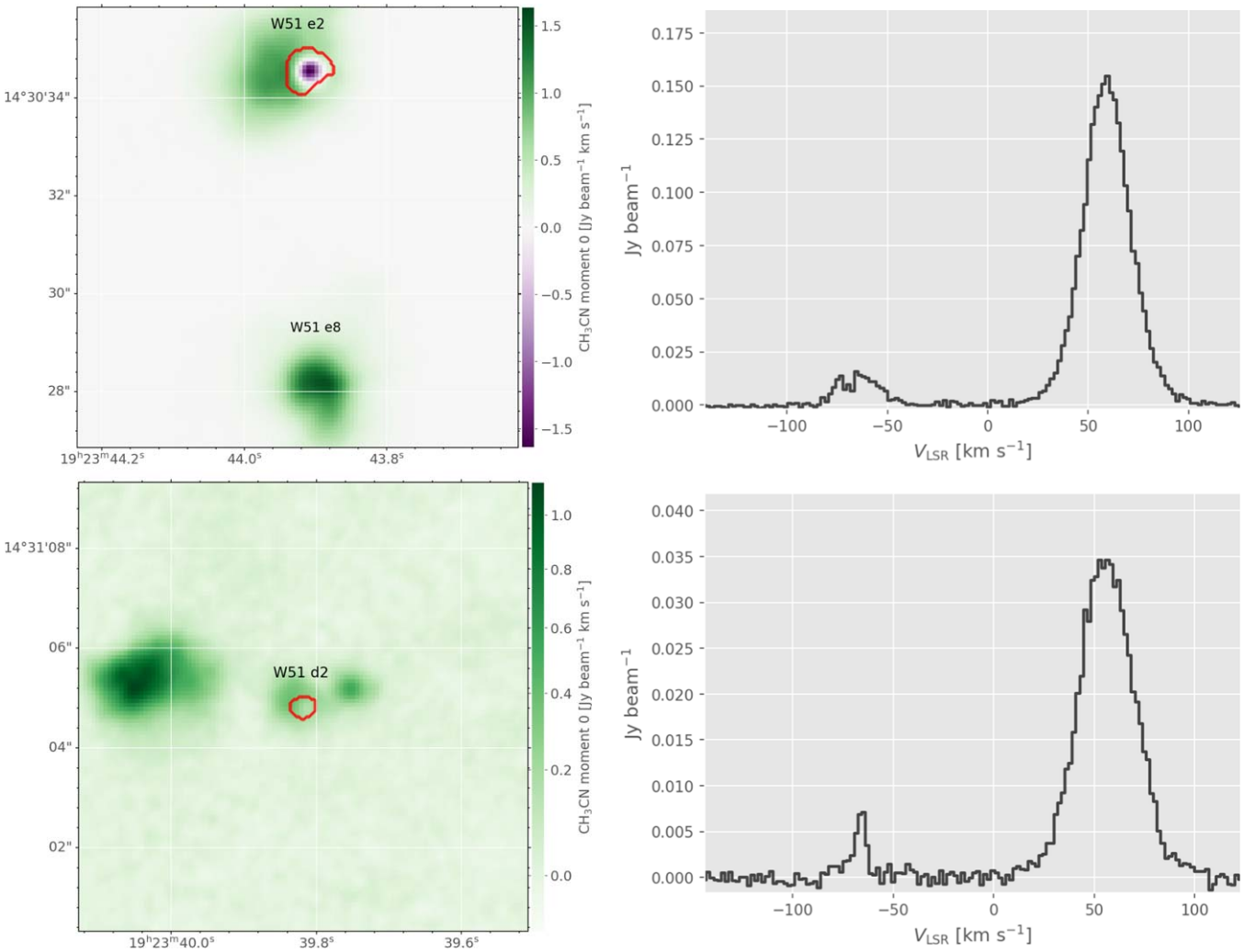

Figure 4. A detailed look at the areas labeled as "bright outliers" (red points) in Figure 3. The top left panel shows the outliers at the position of the well-known HC H II region W51 e2. The CH_3CN line is seen in absorption at this location due to the high brightness temperature of the partially optically thick H II emission. The bottom left panel shows the location of the outliers at the position of the UC H II region W51 d2, which is not as bright in the millimeter continuum; therefore CH_3CN is not seen in absorption. The right panels plot the corresponding H41α and He41α spectra inside the red contours, showing that molecular-line contamination is not significant. Therefore, the most likely origin of the bright outliers is an underestimation of the free–free extrapolation from centimeter wavelengths.

2003), which corresponds to H II region 2 at the southern border of the field of view. Therefore, only H II region 1 is considered for the total Q_0 of MM2. After this consideration, MM2 is the young protocluster with the lowest rate of ionizing photons detected in the sample. Also, G351.77 and G327.29 have very similar values for $Q_0 \approx 0.5 \times 10^{47}\,s^{-1}$. In Motte et al. (2022), G327.29 (young) and G351.77 (intermediate) are at the limit between these two evolutionary categories, so their similar ionizing photon rates are consistent with the proposed classification. W51-E is found to have the second largest Q_0 ($7.4 \pm 1.7 \times 10^{48}\,s^{-1}$) among the ALMA-IMF protoclusters. Since free–free emission is produced by a collisional process, the number of ionizing photons necessary to generate the observed radiation depends on the density squared rather than on the total amount of ionized gas. Therefore, the prevalence of bright and very small ($\sim 10^{-2}$ pc) H II regions in W51-E raises its rank among the evolved protoclusters when Q_0 is considered. The opposite situation occurs in G012.80, which has the second largest free–free flux after G333.60. However, this emission is distributed over a rather large area; therefore the required photoionization rate is the smallest among the evolved protoclusters. We note that the absolute evolutionary stage of a protocluster should not be only determined by its ionizing photon rate, but also by its remaining gas reservoir and substructure (e.g., Pouteau et al. 2023; Díaz-González et al. 2023).

5. Helium Abundances

Compared to optical and IR lines, radio recombination lines are free of obscuration and their excitation is simpler (Gordon & Sorochenko 2002). As mentioned in Section 2, the H41α cubes cover the frequencies of the neighboring He41α line. Abundances of helium with respect to hydrogen can be derived under the assumption that for a given quantum number the recombination lines of the different atoms trace the same gas (e.g., Wilson et al. 2009). The main caveat to this method is that the first ionization potentials of these elements are $\chi = 13.6$ and 24.6 eV, respectively. Therefore, this assumption is valid only for massive stars. We calculate the number abundance of singly ionized He to ionized H using the following equation (for a review of the topic, see

Table 2
H II Region Parameters from Free–Free Continuum Estimations

Protocluster H II Region	d (kpc)	$S_{\rm ff,3mm}$ (mJy)	EM ($\times 10^7$ pc cm^{-6})	n_e ($\times 10^4$ cm^{-3})	D (pc)	Q_0 (10^{47} s^{-1})	SpT	Evol.
W43-MM1	5.5	⋯	⋯	⋯	⋯	⋯	⋯	Y
G338.93	3.9	⋯	⋯	⋯	⋯	⋯	⋯	Y
G328.25	2.5	⋯	⋯	⋯	⋯	⋯	⋯	Y
W43-MM2†	5.5	⋯	⋯	⋯	⋯	0.0227 ± 0.0081	⋯	Y
1	5.5	1.38 ± 0.30	0.40 ± 0.14	1.72 ± 0.31	0.014	0.0227 ± 0.0081	B1	⋯
2	5.5	25.5 ± 1.7	0.61 ± 0.18	1.14 ± 0.16	0.047	0.42 ± 0.12	B0.5	⋯
G337.92	2.7	⋯	⋯	⋯	⋯	0.0363 ± 0.0097	⋯	Y
1	2.7	7.68 ± 0.94	0.144 ± 0.045	0.74 ± 0.11	0.026	0.0304 ± 0.0094	B1	⋯
2	2.7	1.48 ± 0.41	0.141 ± 0.056	1.10 ± 0.22	0.012	0.0059 ± 0.0023	B2	⋯
G327.29	2.5	⋯	⋯	⋯	⋯	0.49 ± 0.14	⋯	Y
1	2.5	144.4 ± 3.9	0.199 ± 0.057	0.472 ± 0.067	0.089	0.49 ± 0.14	B0.5	⋯
G351.77	2.0	⋯	⋯	⋯	⋯	0.52 ± 0.15	⋯	I
1	2.0	230 ± 17	0.37 ± 0.11	0.75 ± 0.11	0.066	0.50 ± 0.15	B0.5	⋯
2	2.0	8.9 ± 2.3	0.135 ± 0.051	0.79 ± 0.15	0.022	0.0194 ± 0.0074	B1	⋯
G353.41	2.0	⋯	⋯	⋯	⋯	1.54 ± 0.33	⋯	I
1	2.0	6.0 ± 2.0	0.123 ± 0.055	0.82 ± 0.18	0.018	0.0130 ± 0.0058	B1	⋯
2	2.0	240 ± 13	0.158 ± 0.046	0.391 ± 0.056	0.103	0.52 ± 0.15	B0.5	⋯
3	2.0	461 ± 34	0.81 ± 0.24	1.13 ± 0.17	0.063	1.00 ± 0.29	B0	⋯
G008.67	3.4	⋯	⋯	⋯	⋯	5.5 ± 1.5	⋯	I
1	3.4	834 ± 32	2.40 ± 0.68	1.69 ± 0.24	0.084	5.2 ± 1.5	O9.5	⋯
2	3.4	41.9 ± 3.3	0.338 ± 0.099	0.82 ± 0.12	0.050	0.263 ± 0.077	B0.5	⋯
W43-MM3	5.5	⋯	⋯	⋯	⋯	12.0 ± 3.4	⋯	I
1	5.5	733 ± 12	0.99 ± 0.28	0.71 ± 0.10	0.199	12.0 ± 3.4	O8.5	⋯
G012.80	2.4	⋯	⋯	⋯	⋯	46 ± 12	⋯	E
1	2.4	13490 ± 230	1.12 ± 0.32	0.567 ± 0.080	0.349	42 ± 12	O7	⋯
2	2.4	113 ± 11	0.221 ± 0.066	0.554 ± 0.083	0.072	0.36 ± 0.11	B0.5	⋯
3	2.4	1231 ± 62	0.90 ± 0.26	0.87 ± 0.13	0.118	3.9 ± 1.1	O9.5	⋯
G010.62	5.0	⋯	⋯	⋯	⋯	57 ± 14	⋯	E
1	5.0	3823 ± 64	5.3 ± 1.5	1.73 ± 0.25	0.177	51 ± 14	O7	⋯
2	5.0	89.2 ± 4.5	0.94 ± 0.27	1.22 ± 0.17	0.064	1.19 ± 0.34	B0	⋯
3	5.0	344.4 ± 9.8	1.24 ± 0.35	1.06 ± 0.15	0.110	4.6 ± 1.3	O9.5	⋯
W51-IRS2	5.4	⋯	⋯	⋯	⋯	63 ± 18	⋯	E
1	5.4	3969 ± 36	2.53 ± 0.72	0.94 ± 0.13	0.284	63 ± 18	O6.5	⋯
2	5.4	1.85 ± 0.49	0.65 ± 0.25	2.32 ± 0.45	0.012	0.029 ± 0.011	B1	⋯
W51-E	5.4	⋯	⋯	⋯	⋯	74 ± 17	⋯	I
1	5.4	675 ± 31	13.3 ± 3.8	5.10 ± 0.73	0.051	10.7 ± 3.1	O8.5	⋯
2	5.4	106.4 ± 5.0	1.98 ± 0.57	1.94 ± 0.28	0.053	1.69 ± 0.48	B0	⋯
3	5.4	3717 ± 27	1.52 ± 0.43	0.653 ± 0.092	0.355	59 ± 17	O6.5	⋯
4	5.4	15.4 ± 2.5	3.7 ± 1.2	5.02 ± 0.82	0.015	0.244 ± 0.080	B0.5	⋯
5	5.4	182.6 ± 6.3	1.36 ± 0.39	1.28 ± 0.18	0.083	2.89 ± 0.82	O9.5	⋯
G333.60	4.2	⋯	⋯	⋯	⋯	341 ± 95	⋯	E
1	4.2	10.0 ± 1.6	0.34 ± 0.11	1.06 ± 0.17	0.030	0.095 ± 0.031	B0.5	⋯
2	4.2	4.8 ± 1.0	0.33 ± 0.12	1.23 ± 0.22	0.021	0.046 ± 0.016	B1	⋯
3	4.2	71.2 ± 4.5	0.53 ± 0.15	0.91 ± 0.13	0.065	0.68 ± 0.20	B0	⋯
4	4.2	35200 ± 190	2.38 ± 0.67	0.592 ± 0.084	0.679	338 ± 95	O4	⋯
5	4.2	10.9 ± 1.7	0.33 ± 0.10	1.00 ± 0.16	0.032	0.104 ± 0.034	B0.5	⋯
6	4.2	78.5 ± 4.5	0.46 ± 0.13	0.79 ± 0.11	0.073	0.75 ± 0.22	B0	⋯
7	4.2	79.2 ± 4.4	0.39 ± 0.11	0.69 ± 0.10	0.080	0.76 ± 0.22	B0	⋯
8	4.2	67.2 ± 4.1	0.326 ± 0.094	0.637 ± 0.092	0.080	0.64 ± 0.19	B0	⋯

Note. Columns: (1) protocluster name; (2) distance in kiloparsecs, see Motte et al. (2022); (3) free–free flux at 98.5 GHz; (4) emission measure; (5) average electron density; (6) source diameter; (7) hydrogen-ionizing photon rate; (8) spectral type from Martins et al. (2005) for O-type stars, and from Panagia (1973) for B-type stars; (9) evolutionary stage from Motte et al. (2022). †Only H II region 1 in Figure 2 corresponds to W43-MM2. H II region 2 corresponds to the region known as MM13, south of MM2 (Motte et al. 2003). Error calculations include the assumed 20% error in T_e, which often dominates over the S/N in the photometry. Errors are reported to two significant figures.

Roelfsema & Goss 1992):

$$\frac{N_{\rm H^+}}{N_{\rm He^+}} = \frac{\int {\rm H}_{41\alpha} dv}{\int {\rm He}_{41\alpha} dv} \approx \frac{N_{\rm H}}{N_{\rm He}}. \quad (6)$$

Given the very large potential for the second ionization of Helium $\chi_{\rm He^+} = 54.40$ eV, this equation also assumes that in the H II gas the number ratio of ionized hydrogen to singly ionized helium is approximately equal to their total elemental abundance ratio.

For each protocluster, we calculated average abundances in the masks used to define the H II regions shown in Figure 2, and with properties reported in Table 2. We performed Gaussian fitting using `Pyspeckit` (Ginsburg et al. 2022a). The spectra were converted to units of brightness temperature as a function of the LSR velocity prior to the fitting. We use the H41α cubes without primary-beam correction to have a noise closer to spatially uniform. This means that the brightness scale of the fitted lines (see Figure 5) is not corrected, but this does not affect the measured abundances, which depend on the line ratio within the mask. An initial round of fitting included only the hydrogen recombination line, and helium was added later using as initial guesses the parameters of the first fitting. For the relative He-to-H brightness, we took as an initial guess a helium-to-hydrogen number abundance $N_{\rm He}/N_{\rm H} = 0.08$ (see Equation (1)), characteristic of the ISM in the Milky Way (Méndez-Delgado et al. 2020).

The intrinsically fainter He41α line at 92.071938 GHz can be more easily affected by molecular-line contamination. If present, the main contaminants are lines of CH_3OCHO at 92.07402 GHz (ortho) and 92.073101 GHz (para). To avoid this contamination in the results, we rejected He41α fits with a peak brightness >0.3 of the hydrogen peak. Additionally, we rejected results with a He41α centroid outside a range of ± 10 km s^{-1} of its theoretical position at -122.17 km s^{-1} from the H41α. These criteria were found empirically (see Figures 5 and 11). We also attempted fits with the C41α component. Valid fits including C41α were found occasionally, but the extra fitted parameters had low signal-to-noise ratio (S/N) and did not improve the overall fit quality. The carbon line is expected to be fainter and is only blueshifted by -27.42 km s^{-1} with respect to helium. Also, its smaller ionization potential (11.3 eV) compared to hydrogen causes this line to be preferentially detected in photon-dominated regions (Wyrowski et al. 1997; Roshi et al. 2005), and not necessarily in H II regions. The final fits only consider hydrogen and helium lines. These are shown in Figure 5 for the H II region in each of the 12 detected protoclusters with the highest average brightness. Figure 11 in Appendix C shows the rest of the H II regions.

It is worth mentioning that although a Gaussian is a good model for most spectra, a few lines show excess or line wings. In the higher-S/N spectra (peak $T_{\rm B} > 1$ K), G333.60 H II 4 (blueshifted) and W51-E H II 1 (redshifted) show the clearest wings. G10.62 H II 1 (redshifted), G12.80 H II 1 (redshifted), G333.60 H II 6 (blueshifted), and W51-IRS2 H II 1 (blueshifted) also show milder wings. Apart from these, W43-MM2 H II 2 (MM13) is a double-peaked line.

Figure 6 shows the helium-to-hydrogen number abundance ratio $N_{\rm He}/N_{\rm H}$ derived for the 25 H II regions in the 11 protoclusters for which $N_{\rm He}/N_{\rm H}$ was measured (see Table 3). Note that the values that we report are relative number abundances. Appendix D clarifies the relation between our measurements and the often used relative He abundance per unit mass Y. A recent analysis using optical recombination lines of H II regions in the Milky Way reports typical values of the quantity $12 + \log(N_{\rm He}/N_{\rm H})$ in the range from 10.9 to 11.0 (Méndez-Delgado et al. 2020), or $N_{\rm He}/N_{\rm H} \approx 0.08$ to 0.1. This range is broadly consistent with our measurements in the UC H II regions within the ALMA-IMF protoclusters.

A few massive star formation regions have been reported to have number He abundances significantly offset from 0.1, from $\sim$0.01 to $\gtrsim$0.3 (Roelfsema & Goss 1992; De Pree et al. 1997). However, previous determinations have been usually done at centimeter wavelengths with less sensitive observations.[24] Within our sample, there are two clear outliers with $N_{\rm He}/N_{\rm H}$ beyond 3σ of the 0.08 to 1 range, both of them on the lower abundance side: H II region 2 in G010.62 with 0.028 ± 0.012, and H II region 3 in G012.80 with 0.045 ± 0.005 (region 2 is at 2.2σ). Their faint He41α emission compared to hydrogen can be seen in Figure 11 for the former and Figure 5 for the latter. A proposed explanation for the apparent detection of small He abundances is a geometric effect, in which the He-ionized gas occupies a smaller volume than the H-ionized gas due to the larger ionization potential of helium (Roelfsema & Goss 1992; De Pree et al. 1997). This effect is less pronounced in resolved observations such as ours, but it could still be relevant. The derived spectral types for the ionizing stars of these H II regions are O9.5 or later (see Table 2); therefore, it is plausible that a softer stellar spectrum in these regions is responsible for the comparatively smaller amounts of ionized helium.

On the high end of the helium abundances, only H II region 2 in W43-MM2 (also known as W43-MM13; see Section 4) is above 1σ from 0.1, with $N_{\rm He}/N_{\rm H} = 0.187 \pm 0.058$. We consider this region as a large-He-abundance candidate, also considering its other special characteristics. The spectrum of this source also has the broadest H41α line among the sample (43.0 ± 1.7 km s^{-1}; see Table 3), and it is clearly double-peaked (see Figure 5). We propose that the ionized gas in this source could be produced by a stellar wind enriched by nuclear-processed products. It is known that massive stars can enrich the ISM with extra amounts of He and metals via powerful stellar winds (Crowther 2007), but it is unclear if these phenomena can exist at the $\sim$ZAMS stages that we are probing. Finally, we note that H II regions 1 and 2 in W51-E have a bright line at the expected position of He41α (see Figure 11). Our fitting procedure rejected it due to molecular-line contamination, most likely from CH_3OCHO lines (see the previous explanation in this section).

6. Discussion

6.1. On the Subtraction of Free–Free Contamination in (Sub)millimeter Observations of the Dust Continuum

Any millimeter survey aimed at studying dust continuum emission has the issue of potential free–free contamination. This becomes more relevant with the availability of sensitive observations of the innermost parts of star-forming cores and young stellar objects, where free–free emission from ionized jets, photoevaporating disks, and the birth of H II regions are expected to contribute to the observed flux (e.g., van der Tak & Menten 2005; Carrasco-González et al. 2012; Rota et al. 2024).

There are three main observational methods to estimate the free–free contribution in millimeter maps: (i) the most common

[24] The brightness of radio and (sub)millimeter recombination lines scales almost linearly with the frequency (e.g., Peters et al. 2012).

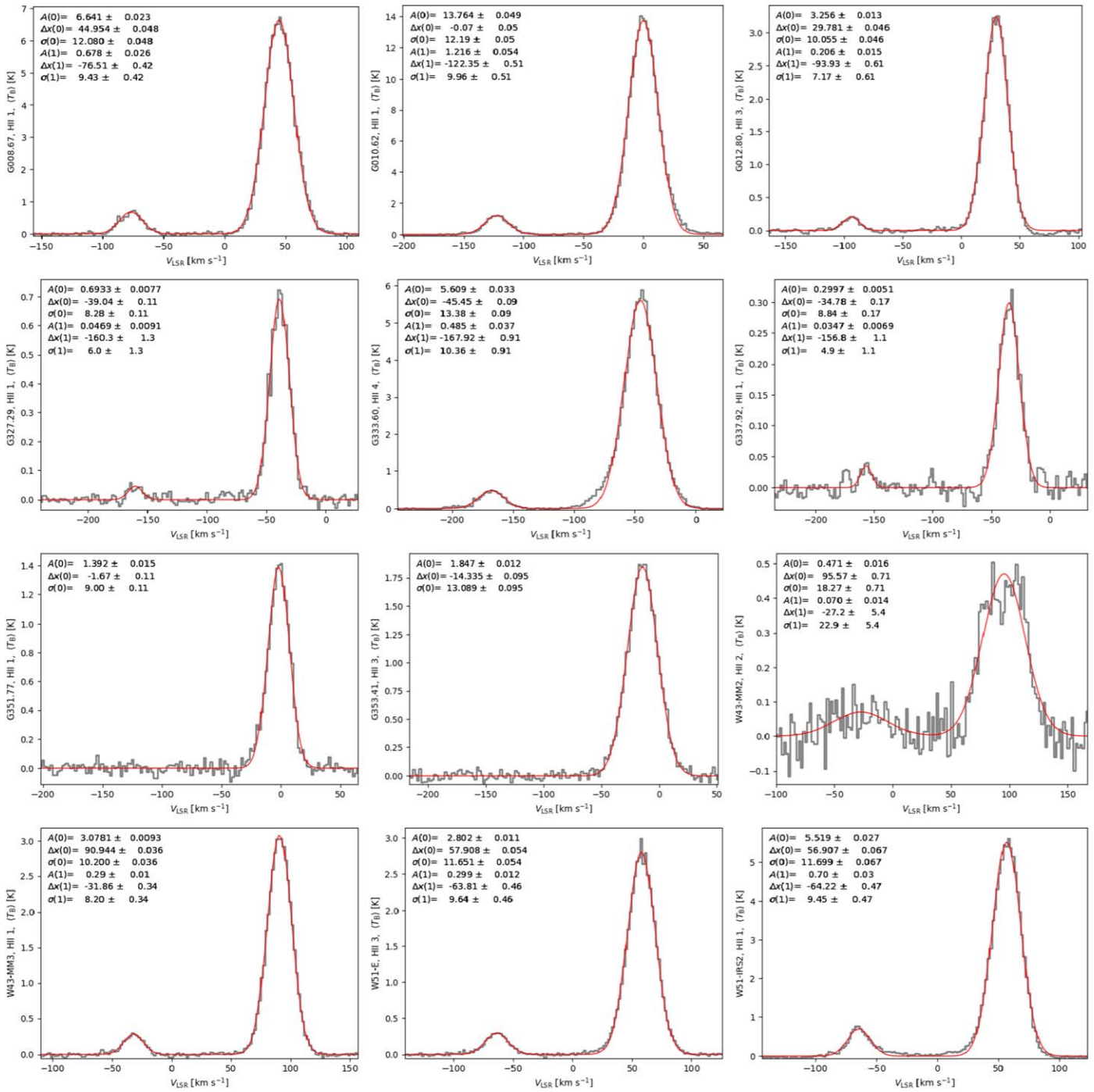

Figure 5. Fits to H41α ($\nu_0 = 92.034434$ GHz) and He41α ($\nu_0 = 92.071938$ GHz) recombination line emission in the 12 protoclusters with detection. This figure shows the brightest region for each protocluster. The rest of the fits are shown in Figure 11 in the Appendix. The fitted parameters and derived abundances are listed in Table 3.

method is using centimeter-wavelength images taken with, e.g., the VLA, and extrapolating them to the millimeter assuming a spectral index $\alpha_{\rm ff}$ for the free–free emission. This method usually assumes $\alpha_{\rm ff} = -0.1$, characteristic of the optically thin regime (see Section 3.3); (ii) creating spectral index α maps between two continuum bands, or measuring α within a given aperture. Free–free emission has a spectral index $\alpha_{\rm ff}$ that changes from 2 to -0.1 as frequency increases and the emission transitions from optically thick to thin. In contrast, the spectral index of dust emission in the radio and (sub)millimeter $\alpha_{\rm dust}$ has the opposite behavior with frequency; it changes from $\lesssim 4$ (optically thin) to 2 (thick) with increasing frequency. These opposite trends with frequency enable to creation of spectral index masks to exclude dust cores that are significantly contaminated by free–free (e.g., Pouteau et al. 2022). Díaz-González et al. (2023) provided spectral index maps sensitive to extended emission between 3 mm and 1 mm, using their combination of the ALMA-IMF continuum maps and single-dish surveys. This method, however, does not provide an estimate of the free–free emission in intensity units, but rather serves as a rejection filter to separate contaminated from noncontaminated areas; and (iii) the method that is systematically used in this paper.

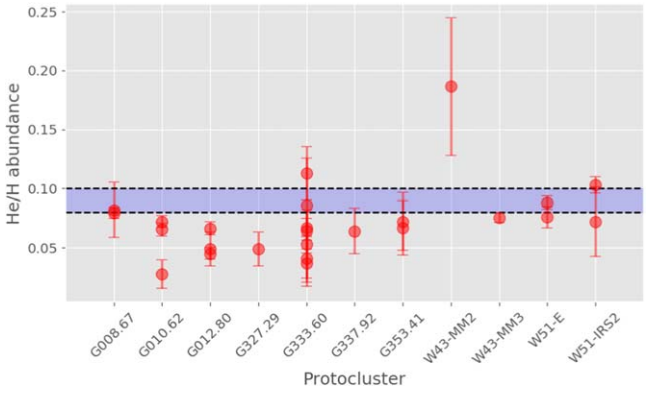

Figure 6. Number abundance of helium with respect to hydrogen $N_{\rm He}/N_{\rm H}$ for the H II regions in the 11 ALMA-IMF protoclusters with detection H41α and He41α. The shaded area within dashed lines marks the expected range for the Milky Way ISM, 0.08 to 0.1.

The main advantages of estimating the free–free contribution with our method are that all the surveyed protoclusters are observed with a (u, v) coverage and beam size close to the continuum images and that the subsequent frequency scaling factor of the free–free estimation is more accurate and numerically closer to 1 (see Section 3.3).

However, our proposed method has its own caveats, namely: (i) the free–free map derived from the recombination line is less sensitive than the corresponding millimeter continuum image. Therefore, it is not able to detect the faintest ionized emission that could be present in the continuum maps; (ii) the H41α emission is assumed to be in LTE. This is a good assumption for most conditions; and (iii) molecular-line contamination of the recombination line emission can be an issue in a few very line-rich objects objects (e.g., Law et al. 2021; Brouillet et al. 2022).

6.2. A Search for Sites with Excess Recombination Line Emission

In this section, we look for regions within the ALMA-IMF images where the H41α line could be brighter than the LTE expectation. There is evidence for the rare occurrence of (mostly weak) recombination line masers in massive star formation regions. The massive young star MonR2-IRS2 has a (sub)millimeter maser with an amplification factor in the range of 2–3 with respect to LTE (Jiménez-Serra et al. 2020). This type of maser is expected to occur in the (sub)millimeter range if the density conditions are appropriate (Walmsley 1990; Peters et al. 2012; Zhu et al. 2022).

We looked for areas in our maps that could be the sites of amplification of the H41α line. For this, we inspected the pure-dust estimation maps (total intensity minus free–free maps after convolution and regridding; see Section 3.1) and looked for areas that are significantly negative, i.e., that have negative "potholes." A naive interpretation of those potholes would be that they are regions where the H41α is brighter than the LTE assumption in Equation (1). We applied the following criteria for our search: (i) that the pothole is clearly visible both in the Band 3 and Band 6 subtraction (pure dust) maps; (ii) that the Band 3 and Band 6 potholes have an area larger than one beam size (this is to avoid negative fluctuations of a few pixels in size); and (iii) that the absolute value of the pothole minimum is larger than the respective error in the free–free estimation, both in Band 3 and Band 6.

We found that when the respective error maps are taken into account (third criterion above), all the cases of potholes are consistent with zero. Therefore, we do not consider them of high significance. Figure 7 shows the case of G010.62, where a clear "pothole" is seen at the position of the well-known UC H II region at the center (e.g., Keto & Wood 2006; Galván-Madrid et al. 2023). This target was our clearest candidate, yet the central hole is within 1σ of the free–free estimation error at that position. We conclude that there is no significant evidence for H41α masers in the ALMA-IMF data and that the areas where the continuum appears to be oversubtracted, notably in the 3 mm maps, are due to the inherent uncertainties in the derivation of the free–free estimations (see Equations (1) and (2)).

6.3. Evolution of the H II Regions in the ALMA-IMF Sample

The ALMA-IMF targets were selected to sample the evolutionary stages of massive star formation in clusters, from quiescent clumps that are faint in the infrared bands and lack ionized gas, to active clumps with prominent H II regions (Motte et al. 2022). Using H41α cubes, we calculated the basic physical properties of their H II regions, such as their EMs, electron densities (n_e), and hydrogen-ionizing photon rates (Q_0). For the H II regions reported in Table 2, Figure 8 shows these properties as a function of the effective diameter D of the emission. Q_0 is well correlated with D, with a Pearson correlation coefficient r and p-value $(r,\ p) = (0.89,\ 1.6 \times 10^{-12})$. In contrast, the correlations between n_e and EM with D are not as clear, with $(r,\ p) = (-0.25,\ 0.15)$ and $(0.12,\ 0.50)$, respectively. A weighted least-squares fit to the Q_0 versus D relation gives $\log[Q_0/{\rm s}^{-1}] = (2.49 \pm 0.18) \times \log[D/{\rm pc}] + (49.89 \pm 0.23)$.

From Equation (5), the observed $Q_0 \propto D^{2.5}$ relation falls in between the expected relations if n_e or EM were constant among the sample of H II regions ($Q_0 \propto D^3$ or $Q_0 \propto D^2$, respectively). Motivated by this, we fit a posteriori the n_e versus D and EM versus D relations in logarithmic space and find that their respective slope and intercept, with 1σ errors, are $(-0.23 \pm 0.08,\ 3.70 \pm 0.10)$ and $(0.52 \pm 0.17,\ 7.39 \pm 0.22)$. Taking $Q_0 \propto D^{2.5}$ as valid, it is indeed expected that $n_e \propto D^{-0.25}$ and ${\rm EM} \propto D^{0.5}$.

Previous authors have reported inverse correlations between n_e and D in samples of UC H II regions, with power-law slopes ≈ -1 (e.g., Garay & Lizano 1999; Kim & Koo 2001). If the ionizing stars had constant Q_0 across the sample, then $n_e \propto D^{-1.5}$ is expected. However, there is no reason to think that all UC H II regions will be ionized by stars of the same mass at the moment of observation and to follow the same path on the n_e versus D diagram as they expand and rarefy. A possible cause for our differing results with respect to previous surveys is that those have focused on the brightest UC H II regions within rather evolved targets, selected from their mid-IR colors (e.g., Wood & Churchwell 1989; Kurtz et al. 1994). In contrast, the UC H II regions in our sample are distributed in a broad range of protocluster evolutionary stages, and in different locations within a given protocluster. A homogeneous analysis of a larger sample could help to understand this issue. As pointed out by Garay & Lizano (1999), a positive correlation in the Q_0 versus D diagram (bottom panel of Figure 8) indicates that the smallest UC H II regions are on

Table 3
Fitted Parameters for H41α and He41α

Protocluster H II Region	H41α A (K)	H41α $v_{\rm LSR}$ (km s^{-1})	H41α FWHM (km s^{-1})	He41α A (K)	He41α $v_{\rm LSR}$ (km s^{-1})	He41α FWHM (km s^{-1})	$N_{\rm He}/N_{\rm H}$
G008.67 1	6.64 ± 0.023	44.954 ± 0.048	28.45 ± 0.11	0.678 ± 0.026	−76.51 ± 0.42	22.20 ± 0.98	0.0797 ± 0.0047
G008.67 2	0.930 ± 0.016	41.05 ± 0.19	22.52 ± 0.44	0.093 ± 0.017	−79.1 ± 1.7	18.4 ± 3.9	0.082 ± 0.023
G010.62 1	13.764 ± 0.049	−0.073 ± 0.050	28.69 ± 0.12	1.216 ± 0.054	−122.35 ± 0.51	23.4 ± 1.2	0.0722 ± 0.0049
G010.62 2	2.451 ± 0.021	5.916 ± 0.089	21.34 ± 0.21	0.076 ± 0.022	−117.5 ± 2.7	19.1 ± 6.4	0.028 ± 0.012
G010.62 3	4.451 ± 0.017	−0.874 ± 0.041	22.002 ± 0.096	0.337 ± 0.018	−123.38 ± 0.50	19.1 ± 1.2	0.0656 ± 0.0054
G012.80 1	3.162 ± 0.012	36.752 ± 0.058	30.48 ± 0.14	0.233 ± 0.013	−86.13 ± 0.75	27.6 ± 1.8	0.0665 ± 0.0056
G012.80 2	1.020 ± 0.012	36.44 ± 0.12	19.56 ± 0.28	0.084 ± 0.016	−85.7 ± 1.1	11.6 ± 2.6	0.049 ± 0.014
G012.80 3	3.256 ± 0.013	29.781 ± 0.046	23.68 ± 0.11	0.206 ± 0.015	−93.93 ± 0.61	16.9 ± 1.4	0.0452 ± 0.0051
G327.29 1	0.6933 ± 0.0077	−39.04 ± 0.11	19.50 ± 0.25	0.0469 ± 0.0091	−160.3 ± 1.3	14.1 ± 3.1	0.049 ± 0.014
G333.60 1	0.685 ± 0.021	−46.45 ± 0.41	27.40 ± 0.96	…	…	…	…
G333.60 2	0.593 ± 0.015	−47.09 ± 0.29	22.94 ± 0.68	0.050 ± 0.015	−169.0 ± 3.5	23.5 ± 8.2	0.086 ± 0.040
G333.60 3	1.961 ± 0.022	−44.77 ± 0.11	20.43 ± 0.27	0.158 ± 0.025	−163.9 ± 1.3	16.4 ± 3.0	0.065 ± 0.016
G333.60 4	5.609 ± 0.033	−45.446 ± 0.090	31.52 ± 0.21	0.485 ± 0.037	−167.92 ± 0.91	24.4 ± 2.2	0.0670 ± 0.0078
G333.60 5	0.5027 ± 0.0092	−33.13 ± 0.18	20.54 ± 0.44	0.041 ± 0.013	−154.6 ± 1.6	10.3 ± 3.8	0.041 ± 0.020
G333.60 6	0.953 ± 0.017	−50.49 ± 0.22	24.85 ± 0.52	0.072 ± 0.025	−173.4 ± 2.1	12.1 ± 4.8	0.037 ± 0.019
G333.60 7	0.913 ± 0.017	−45.54 ± 0.20	21.86 ± 0.47	0.048 ± 0.017	−166.9 ± 3.9	22.2 ± 9.1	0.053 ± 0.029
G333.60 8	0.679 ± 0.010	−44.61 ± 0.17	22.47 ± 0.39	0.082 ± 0.011	−166.1 ± 1.3	20.9 ± 3.1	0.113 ± 0.022
G337.92 1	0.2997 ± 0.0051	−34.78 ± 0.17	20.82 ± 0.41	0.0347 ± 0.0069	−156.8 ± 1.1	11.5 ± 2.6	0.064 ± 0.019
G337.92 2	0.2190 ± 0.0063	−32.74 ± 0.30	21.23 ± 0.71	…	…	…	…
G351.77 1	1.392 ± 0.015	−1.67 ± 0.11	21.19 ± 0.27	…	…	…	…
G351.77 2	0.561 ± 0.083	−9.8 ± 1.2	16.5 ± 2.8	…	…	…	…
G353.41 1	0.3239 ± 0.0073	−17.00 ± 0.22	20.38 ± 0.53	0.046 ± 0.010	−137.1 ± 1.1	10.3 ± 2.6	0.072 ± 0.025
G353.41 2	0.5077 ± 0.0079	−16.11 ± 0.20	25.50 ± 0.46	0.0366 ± 0.0082	−139.6 ± 2.6	23.7 ± 6.2	0.067 ± 0.023
G353.41 3	1.847 ± 0.012	−14.335 ± 0.095	30.82 ± 0.22	…	…	…	…
W43-MM2 1	0.96 ± 0.17	92.0 ± 2.3	26.6 ± 5.5	…	…	…	…
W43-MM2 2	0.471 ± 0.016	95.57 ± 0.71	43.0 ± 1.7	0.070 ± 0.014	−27.2 ± 5.4	54 ± 13	0.187 ± 0.058
W43-MM3 1	3.0781 ± 0.0093	90.944 ± 0.036	24.018 ± 0.084	0.289 ± 0.010	−31.86 ± 0.34	19.31 ± 0.80	0.0755 ± 0.0041
W51-E 1	16.81 ± 0.13	59.17 ± 0.10	27.13 ± 0.25	…	…	…	…
W51-E 2	3.794 ± 0.052	56.35 ± 0.15	21.87 ± 0.34	…	…	…	…
W51-E 3	2.802 ± 0.011	57.908 ± 0.054	27.44 ± 0.13	0.299 ± 0.012	−63.81 ± 0.46	22.7 ± 1.1	0.0882 ± 0.0056
W51-E 4	1.485 ± 0.045	51.79 ± 0.42	27.95 ± 0.98	…	…	…	…
W51-E 5	2.458 ± 0.017	67.307 ± 0.076	21.93 ± 0.18	0.273 ± 0.021	−53.68 ± 0.56	15.0 ± 1.3	0.0758 ± 0.0089
W51-IRS2 1	5.519 ± 0.027	56.907 ± 0.067	27.55 ± 0.16	0.704 ± 0.030	−64.22 ± 0.47	22.2 ± 1.1	0.1030 ± 0.0069
W51-IRS2 2	1.144 ± 0.038	48.90 ± 0.46	28.1 ± 1.1	0.256 ± 0.067	−71.5 ± 1.2	9.1 ± 2.8	0.072 ± 0.029

Note. Columns: (1) protocluster and H II region; (2) and (5) peak intensity of spatially averaged spectrum; (3) and (6) LSR velocity of line peak; (4) and (7) line FWHM. Errors are reported to two significant figures.

average ionized by less massive stars. Therefore, it could be that the smaller H II regions in our sample are not necessarily dynamically younger, or at least that the effect of the ionizing spectral type is larger than the effect of age. A lack of a direct relation between UC H II region size and other measured properties has been previously proposed as a solution to the apparent (excess) lifetime "problem" of UC H II regions (Peters et al. 2010a, 2010b; De Pree et al. 2014). Another possible explanation for differing results in the n_e versus D relation is the environment. For example, the recent study by Meng et al. (2022) of the UC H II regions in the extreme protocluster Sgr B2 found that n_e and D follow an inverse relation, but with significant scatter and at higher densities than previous studies in other regions. Similarly, Yang et al. (2021) analyzed several samples of UC H II regions and found that their physical properties probably shift with evolution. Finally, the presence or absence of ionized haloes around UC H II regions and the ability of interferometric observations to recover them might have an effect too (Kim & Koo 2001). Figure 8 labels the outliers from the fitted relations. The most notable ones with an excess in n_e, EM, or Q_0 are H II regions 1 and 4 in W51-E, followed by H II region 1 in W43-MM2, 1 in G008.67, and 2 in W51-E. The UC H II regions in the north–south dust ridge of W51-E (which we label 1 and 2) are known to have active infall signatures (e.g., Zhang et al. 1998; Goddi et al. 2016).

We now calculate the corresponding H41α dynamical line widths $\Delta V_{\rm dyn}$. The total recombination line width is a nonlinear sum of collisional ("pressure"), thermal, and dynamical widths

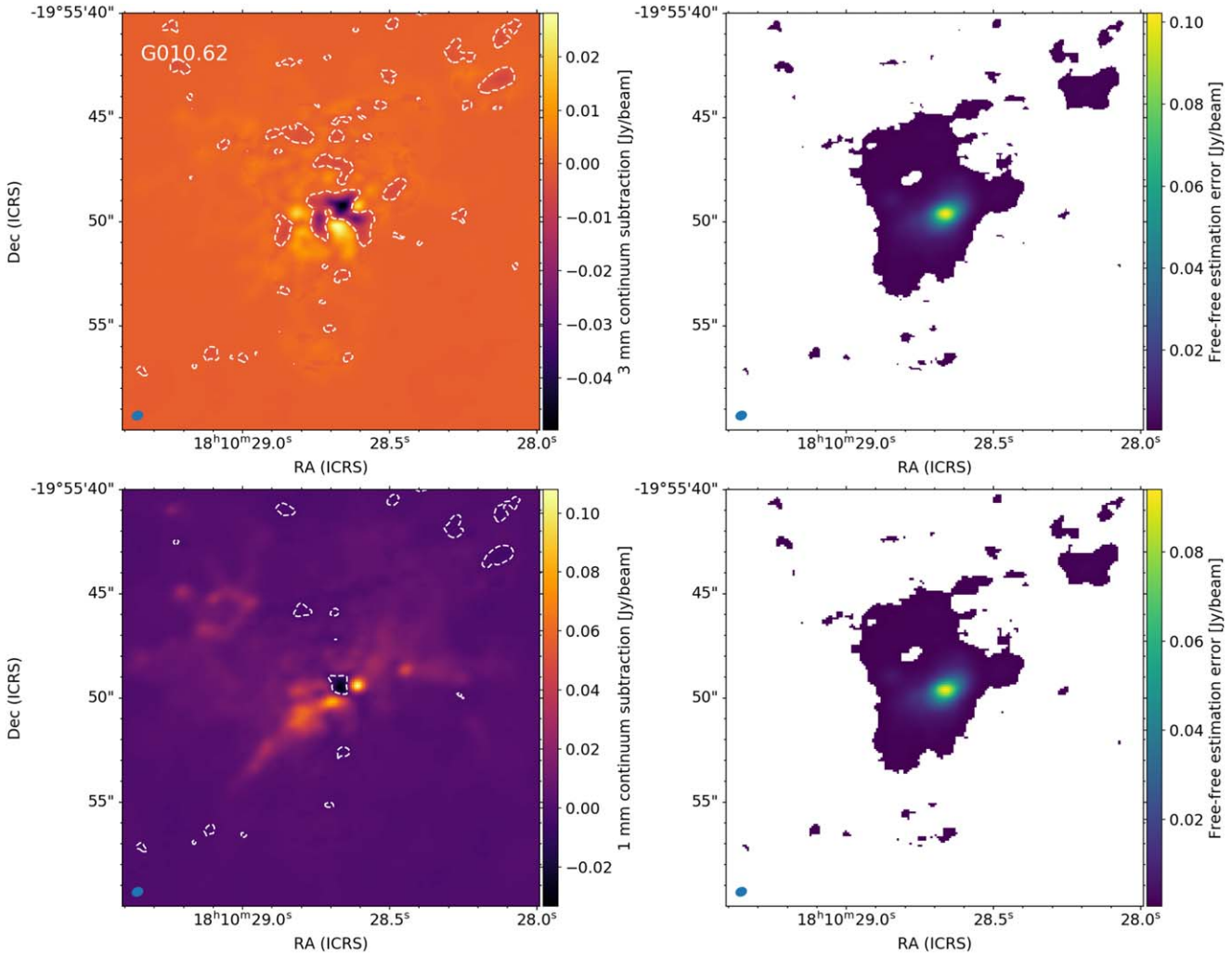

Figure 7. Detailed view of areas of the free–free oversubtraction issue, or negative "potholes" in G010.62. Top panels: 3 mm continuum minus free–free estimation (left) and corresponding error of the free–free estimation (right). Dashed contours are at $-10 \times \sigma_{\rm mad\_std} = -8.2$ mJy beam^{-1}. Bottom panels: B6 continuum minus free–free estimation (left) and corresponding error of the free–free estimation (right). Dashed contours are at $-10 \times \sigma_{\rm mad\_std} = -12.6$ mJy beam^{-1}. "Potholes" in the central UC H II region are present in both the 3 mm and 1 mm subtractions, but the negative peak is still consistent with zero when the error map of the free–free estimation is considered.

(Gordon & Sorochenko 2002; Keto et al. 2008). Following the equations in the appendix of Galván-Madrid et al. (2012), we estimate that collisional broadening is about 0.05 km s^{-1} for densities as high as 10^5 cm^{-3}, therefore it can be neglected. The thermal FWHM line width at $T_e = 7000\,{\rm K} \pm 20\%$ is 17.9 ± 1.8 km s^{-1}. Supersonic recombination lines have been suggested to be a signpost of ultracompact and "hypercompact" H II regions with additional physical ingredients beyond the classical hydrodynamical expansion (e.g., De Pree et al. 2004; Galván-Madrid et al. 2009; Sandell et al. 2009). However, these objects appear to be very rare, including in our survey. Interestingly, $\Delta V_{\rm dyn}$ appears to be weakly correlated both with H II region size (Figure 9, top panel) and ionizing photon rate Q_0 (bottom panel), with $(r, p) = (0.34, 0.05)$ and (0.33, 0.06), respectively. As shown before, H II region size and Q_0 are well correlated; therefore, the trend of increasing dynamical line width with size likely reflects the same underlying physical process. The hydrodynamical expansion velocity of an H II region is expected to be $\lesssim c_s$ (Spitzer 1978; Bisbas et al. 2015), where the speed of sound of ionized gas is $c_s \approx 10$ km s^{-1}. Therefore, an optically thin H II region is expected to have an observed dynamical line width of $\lesssim 2c_s$. Most of the objects in our sample satisfy this, as shown in Figure 9. However, the trend of increasing $\Delta V_{\rm dyn}$ with Q_0 (spectral type), as well as the small excess line width above $2c_{\rm s}$ at high Q_0, suggest that other acceleration mechanisms could play a role at high luminosities. Photoevaporative flows in density gradients, such as those in structured clouds, are able to accelerate H II gas to a few tens of kilometers per second (Arthur & Hoare 2006; Zamora-Avilés et al. 2019). Faster velocities would require the presence of stellar winds. We suggest that this is the case for the H II region south of W43-MM2 (MM13). This H II region stands out with $\Delta V_{\rm dyn} = 39.1 \pm 2.0$ km s^{-1}. An embedded stellar or disk wind (e.g., Guzmán et al. 2020; Galván-Madrid et al. 2023) could produce the observed large line width in this region, as well as in the other outlier objects with $\Delta V_{\rm dyn} > 2c_s$, which are labeled in Figure 9. Finally, we keep in mind that our analysis of helium abundances (see Section 5) revealed that the H II region MM13 also has the largest helium abundance $N_{\rm He}/N_{\rm H} = 0.187 \pm 0.058$ and that the line in this source is the only one which is clearly double-peaked. A full investigation of the ionizing sources requires the observation and modeling of more recombination lines.

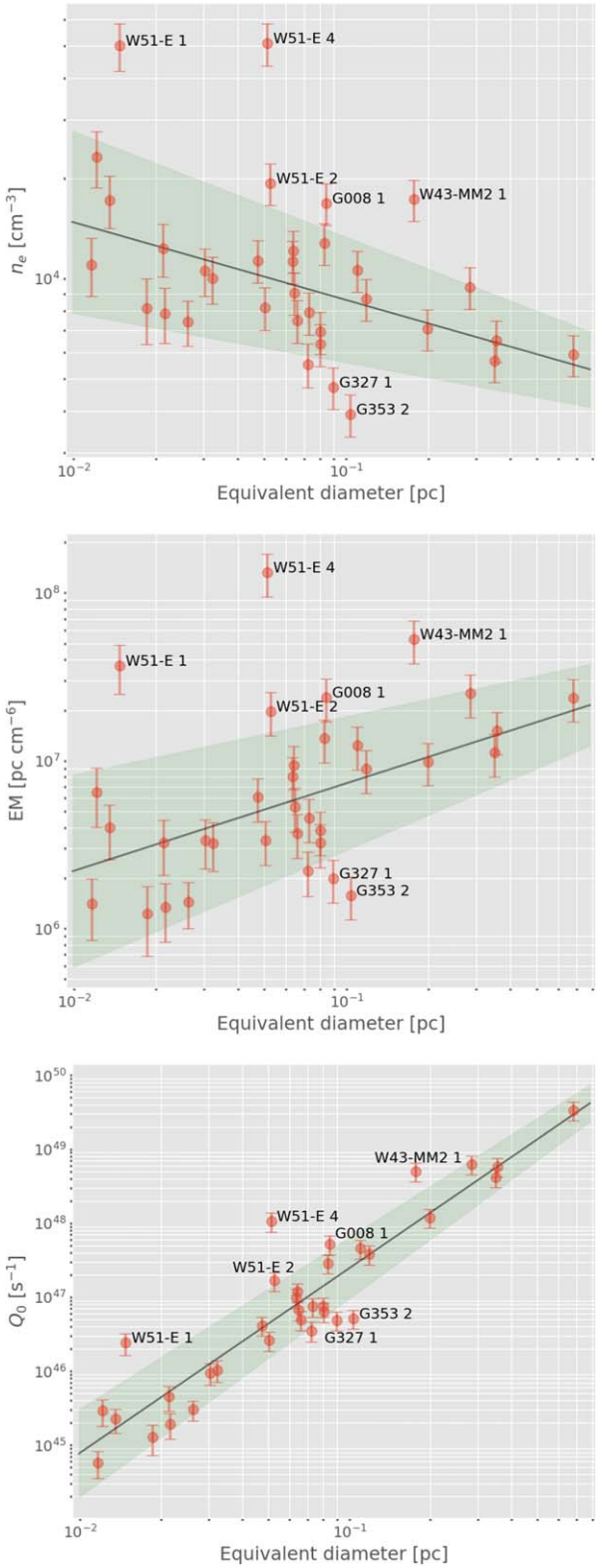

Figure 8. Physical properties of the H II regions in the ALMA-IMF protoclusters listed in Table 2, as a function of their equivalent diameter D. Top panel: electron density n_e, middle panel: emission measure EM, bottom panel: ionizing photon rate Q_0. The black lines and shaded areas show the respective best fits and 1σ confidence intervals. The better constrained linear relation is $\log[Q_0/\mathrm{s}^{-1}] = (2.49 \pm 0.18) \times \log[D/\mathrm{pc}] + (49.89 \pm 0.23)$. The slope and intercept for $\log(n_e)$ vs. $\log(D)$ are -0.23 ± 0.08 and 3.70 ± 0.10. The slope and intercept for log(EM) vs. $\log(D)$ are 0.52 ± 0.17 and 7.39 ± 0.22 (1σ errors). H II regions that are outliers in at least one of their properties are labeled.

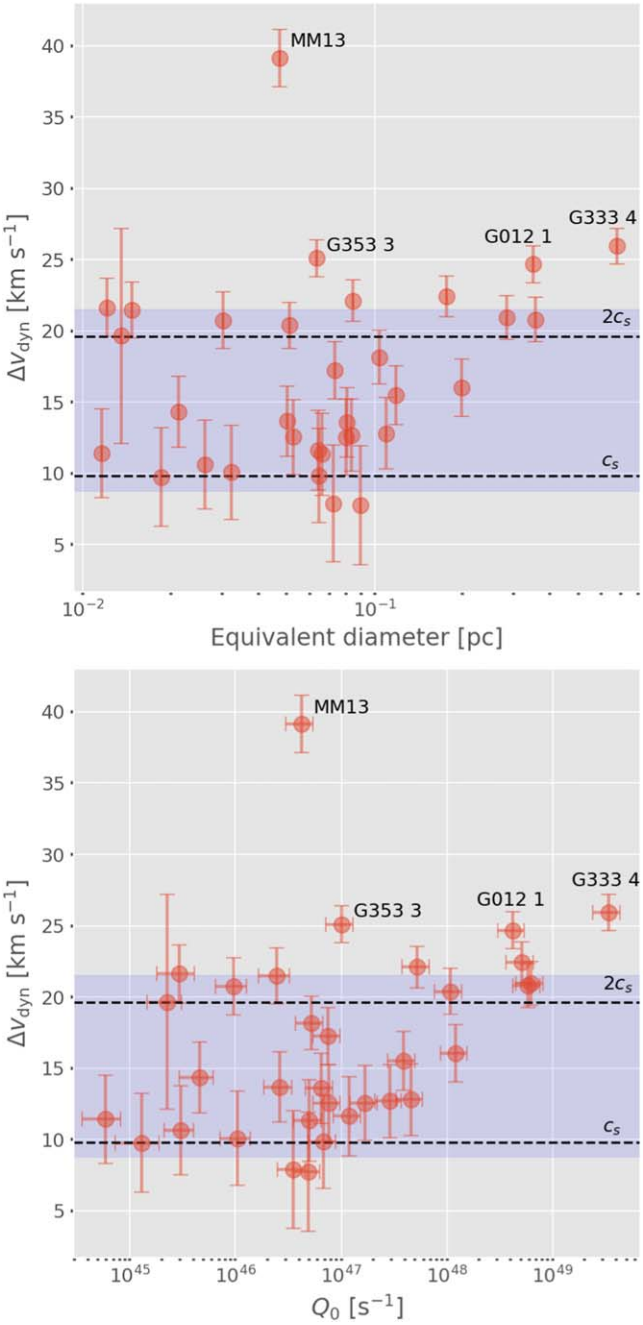

Figure 9. Dynamical FWHM line width (ΔV_{dyn}) of the H41α emission vs. the logarithm of their equivalent diameter (top panel) and of the ionizing photon rate (bottom panel). The plot shows the H II regions in the ALMA-IMF protoclusters listed in Table 2, except for H II region 2 in G351.77, whose total line width is consistent with being purely thermal. The speed of sound of ionized gas at the assumed $T_e = 7000$ K is $c_s = 9.82$ km s^{-1}. Considering a 20% error in Te, the shaded area marks the expected range of H II region expansion velocities between $c_s(T_e - \sigma_{T_e})$ and $2c_s(T_e + \sigma_{T_e})$. Outliers are marked.

7. Conclusions

We made tailored H41α cubes using the ALMA-IMF pipeline (Ginsburg et al. 2022b; Cunningham et al. 2023) to create template maps, and their associated errors, of the free–free emission in the 3 mm and 1.3 mm continuum maps. With this paper, we distribute the input cubes, the derived data products, and associated scripts, which can be used to separate

the free–free "contamination" from dust emission in ALMA continuum maps for other projects.

We validated our procedure against the more common approach of extrapolating the free–free emission from centimeter maps to millimeter wavelengths. For our benchmark region, we found that both approaches give the same result within the errors for the vast majority of the pixels with emission in both tracers, but that they do not necessarily match in a few UC H II regions where either the recombination line can have excess brightness, or the optically thin ($\propto\nu^{-1}$) extrapolation from the centimeter to the millimeter is underestimation. Another possible issue is molecular-line contamination, which we found to be important only in three hot molecular cores.

We used the derived free–free maps to estimate the properties of H II regions across the ALMA-IMF protoclusters. We defined 34 regions of H II emission and measured their photometry. Then, we derived their physical properties such as the EM, electron density (n_e), hydrogen-ionizing photon rate (Q_0), and spectral type (SpT) of the (single) ionizing star. Q_0 and SpT follow a trend consistent with the evolutionary picture proposed by Motte et al. (2022). The youngest protoclusters (W43-MM1, G338.93, G328.25) lack detectable emission from ionized gas. W43-MM2 and G337.92 harbor B-type stars with Q_0 of few $\times 10^{45}\,s^{-1}$ (the MM13 region south of MM2 also contains a more luminous B-type star). G351.77 and G327.29 contain early B-type stars with a total Q_0 of a few $\times 10^{46}\,s^{-1}$. G353.41 and G008.67 have early B to late O-type stars with $Q_0 \sim 10^{47}\,s^{-1}$. The following ALMA-IMF protoclusters, W43-MM3, G012.80, G010.62, W51-IRS2, and W51-E, contain from a few to several O- and B-type stars, with Q_0 rising from $\sim 1\times$ to $7 \times 10^{48}\,s^{-1}$. Finally, G333.60 contains the brightest and largest H II region in the sample, as well as the largest number of OB stars, totaling $Q_0 \approx 3 \times 10^{49}\,s^{-1}$.

We performed measurements of the number abundance of He^+ with respect to H^+, which is a proxy to the total He-to-H abundance N_{He}/N_H in H II regions. Most of the 25 regions with He^+ measurement (see Table 3) have values consistent with the expected $N_{He}/N_H \approx 0.08$ in the Galactic ISM. Two H II regions appear to have helium abundances significantly below this value. We propose that this is due to the relatively late spectral type of their ionizing stars, which produces He^+ regions that are smaller than their respective H^+ regions. Only one H II region (W43-MM13, south of MM2) appears to have N_{He}/N_H above the standard value.

We looked for sites of significant amplification of the H41α with respect to LTE. This search returned negative results when the errors of the free–free estimation maps are considered.

We investigated the possible correlations between the measured H II region properties in the sample. The correlations n_e and equivalent diameter D and between EM and D are weak. In contrast, Q_0 and D are well correlated and have a linear dependence in the log–log space with an exponent of $\approx$2.5. This favors an interpretation where the smaller UC H II regions are not necessarily the less dynamically evolved versions of the larger ones, but rather they are on average ionized by less massive stars. Finally, the dynamical width ΔV_{dyn} of the H II regions in the sample was deconvolved from the thermal and collisional widths, the latter of which is totally negligible. Moderate positive correlations were found between ΔV_{dyn} and D, and between ΔV_{dyn} and Q_0. Dynamical widths vary from approximately the speed of sound of ionized gas c_s to $\gtrsim 2c_s$, with MM13 being again an outlier with $\Delta V_{dyn} \approx 4c_s$. The trend among the sample of increasing ΔV_{dyn} with Q_0 suggests that, in the H II regions ionized by the most massive stars, further mechanisms such as disk or stellar winds could play a role in their kinematics.

Acknowledgments

We thank the anonymous referee for a detailed report, which helped to improve many aspects of this paper. R.G.M., D.D.G., and R.R.S. acknowledge support from UNAM-PAPIIT project IN108822 and from CONACyT Ciencia de Frontera project ID 86372. A.G. acknowledges support from the NSF under grants AST 2008101 and CAREER 2142300. T.Cs. has received financial support from the French State in the framework of the IdEx Université de Bordeaux Investments for the Future Program. A.M.S. gratefully acknowledges support by the Fondecyt Regular (project code 1220610), and ANID BASAL project FB210003. R.A.G. gratefully acknowledges support from ANID Beca Doctorado Nacional 21200897. L.B. gratefully acknowledges support from the ANID BASAL project FB210003.

Software: `Astropy` (Astropy Collaboration et al. 2013, 2018), `PySpecKit` (Ginsburg et al. 2022a), `CASA` (CASA Team et al. 2022), APLpy (Robitaille & Bressert 2012).

Appendix A
Comparison of Original, Free–Free, and Pure-dust Maps

Figure 10 shows comparison plots, covering the areas with free–free emission, of the original 1.3 mm continuum maps and the corresponding free–free and pure-dust estimations.

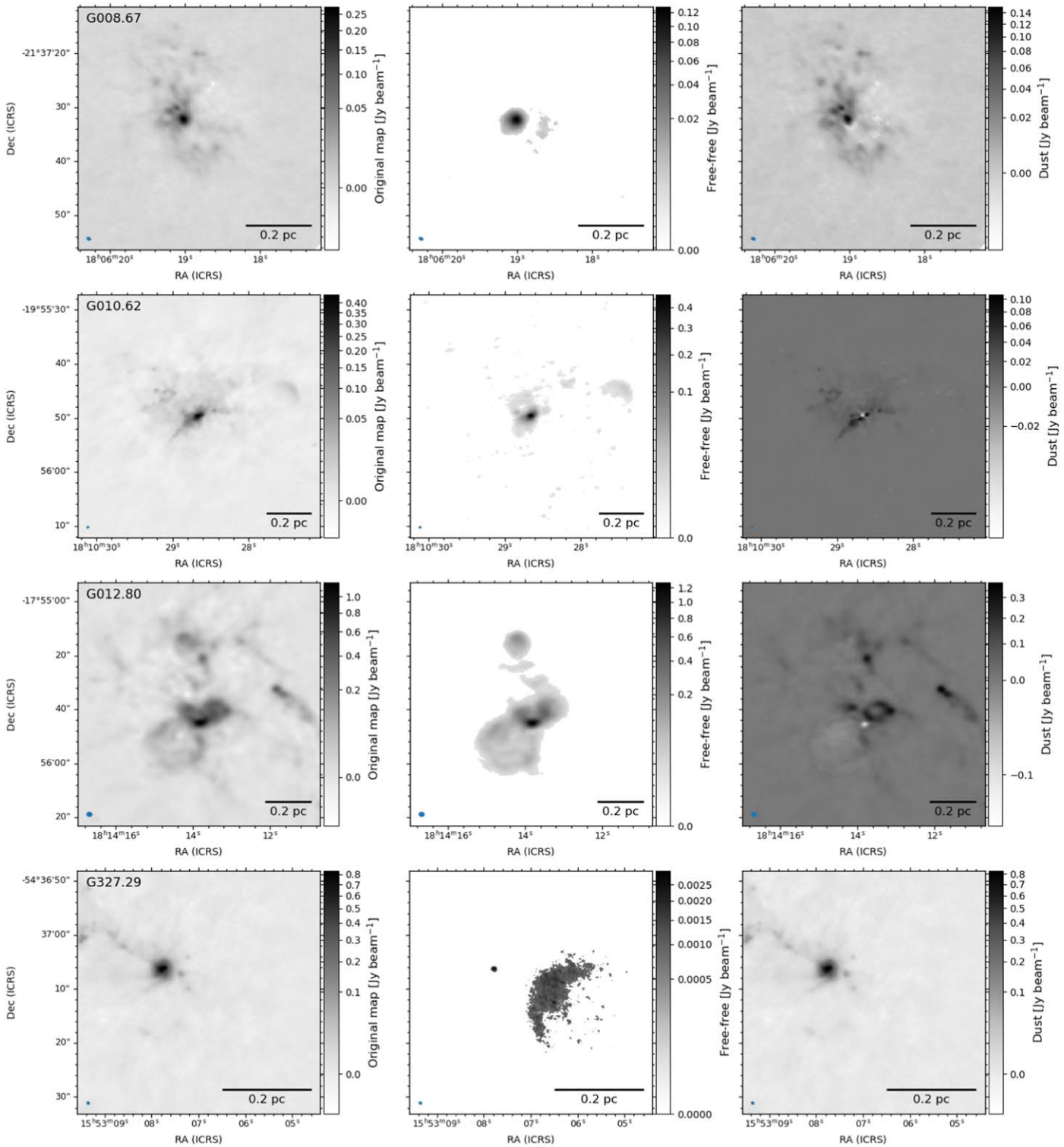

Figure 10. Comparison of the original 1.3 mm continuum image convolved to the angular resolution of the H41α cube (left panel), free–free estimation map at 1.3 mm (center), and the corresponding pure-dust estimation map (right). The images shown are prior to primary-beam correction. The color normalization is a power law with a 0.33 exponent. The displayed areas are the same as in Figure 2 and correspond to where free–free emission was detected.

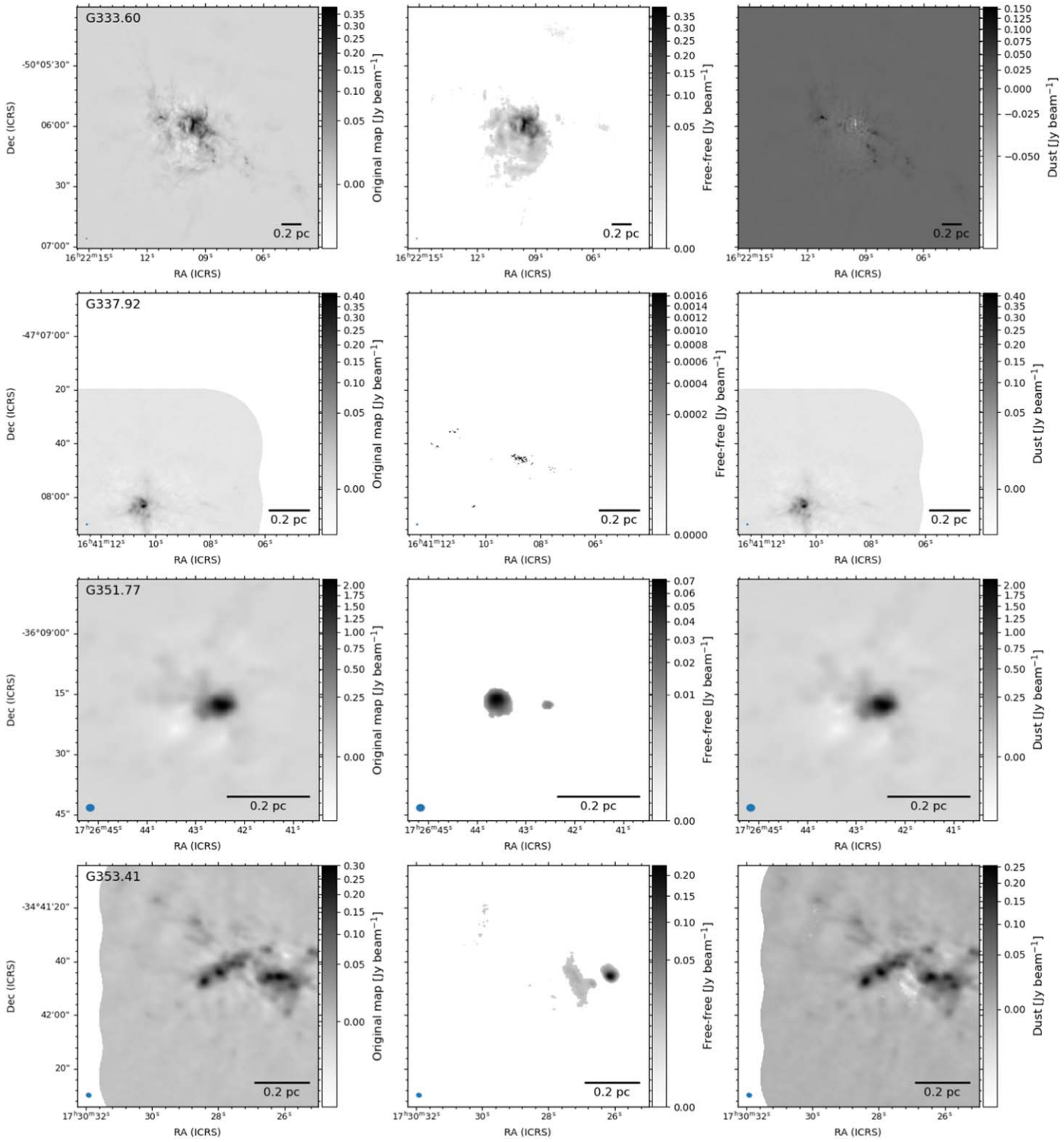

Figure 10. (Continued.)

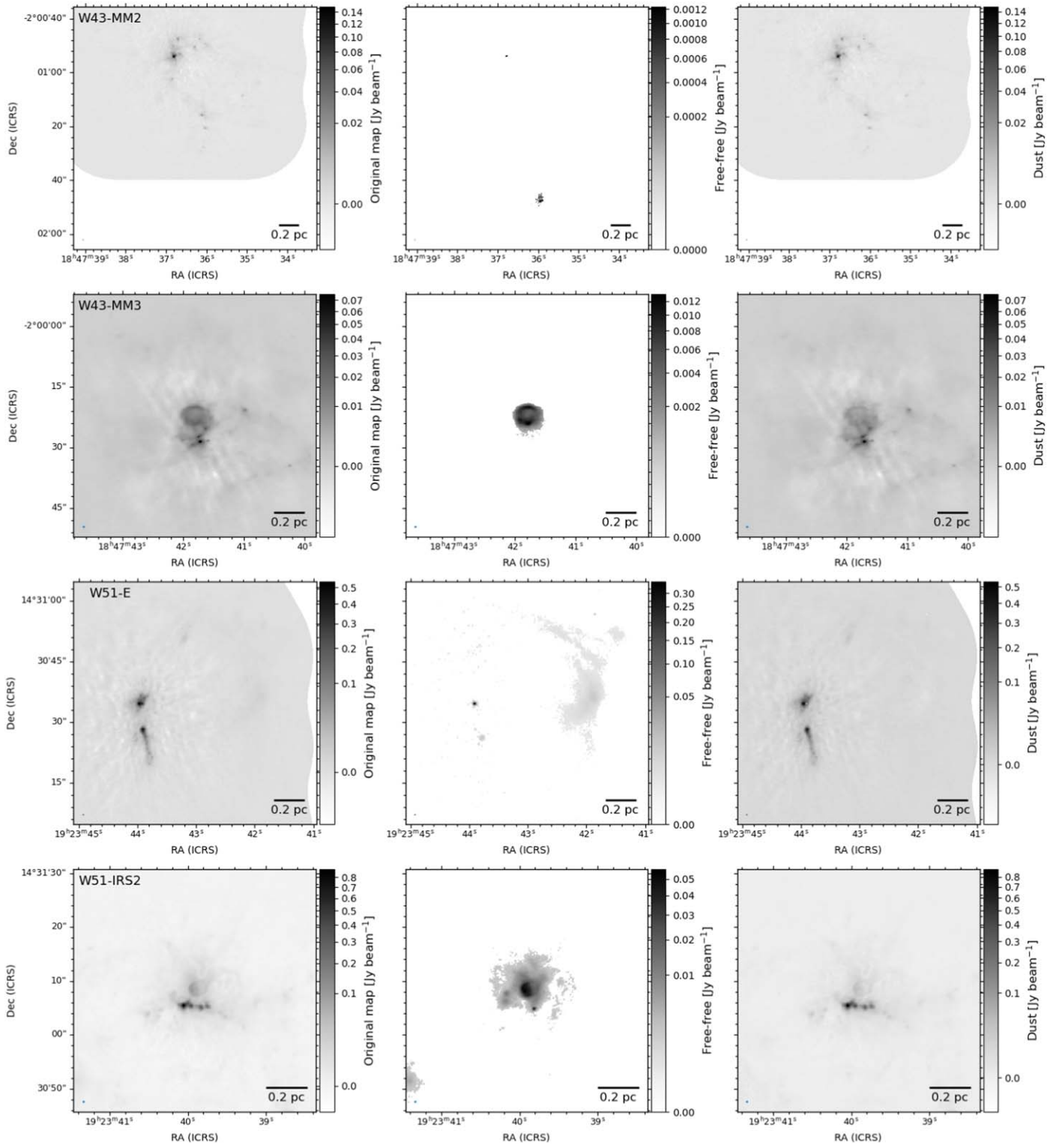

Figure 10. (Continued.)

Appendix B
File Names and Data Products

We make available the following FITS images at https://dataverse.harvard.edu/dataverse/h41a-freefree, hosted by the Harvard Dataverse service (doi:10.7910/DVN/LWILNE).

1. The image cubes containing the hydrogen and helium 41α lines, prior to primary-beam correction (see Section 3.1): `FIELD_B3_spw1_12M_h41a.JvM.image.contsub.fits`.
2. The regridded free–free estimation $I_{\mathrm{ff},\nu}$ for each protocluster at the standard ALMA-IMF `cleanest` continuum frequencies of 98.5 and 224.5 GHz. The file names start with the base name `FIELD_B3_spw1_12M_h41a.JvM.image.contsub`, which is the standard naming within the ALMA-IMF data reduction pipeline (see Ginsburg et al. 2022b). The file names are then followed by `.m0.ffXXX.XGHz_Y.Ysigma.regr`, which denotes the fact that they are obtained from a moment 0 map, the frequency of the calculation, the threshold in the moment 0 map above which Equation (1) is applied, and the applied regridding. Finally, the file names end with either `.pbcor.fits` or just with. `fits`, depending on whether primary-beam correction is applied or not at the end of the procedure (see Figure 1). An example file name with PB correction is `W51-IRS2_B3_spw1_12M_h41a.JvM.image.contsub.m0.ff224.5GHz_5.0sigma.regr.pbcor.fits`.
3. The error σ_{ff} of the free–free estimation. Following the same nomenclature as above but with `.err` in the file name, e.g., `W51-IRS2_B3_spw1_12M_h41a.JvM.image.contsub.m0.ff224.5GHz_5.0sigma.err.regr.pbcor.fits`.
4. The `cleanest` continuum image from the release of Ginsburg et al. (2022b) convolved to the beam size of the H41α cube. The file name is the same as in the ALMA-IMF data release, but ending with `.conv.fits`. For example: `W51-IRS2_B6_uid___A001_X1296_X187_continuum_merged_12M_robust0_selfcal9_finaliter.image.tt0.conv.fits`
5. Estimates of pure-dust continuum emission, from the subtraction of the original continuum images minus the free–free estimations, with and without PB correction. The base names of these images are the same as those of the original continuum images, but ending with `.conv.ffsub_Y.Ysigma.fits`.

Appendix C
Hydrogen and Helium 41α Fitting in the Rest of the H II Regions

In Figure 11 we show the H41α and He41α fitting in the rest of the H II regions defined in Section 4, and not shown in Figure 5.

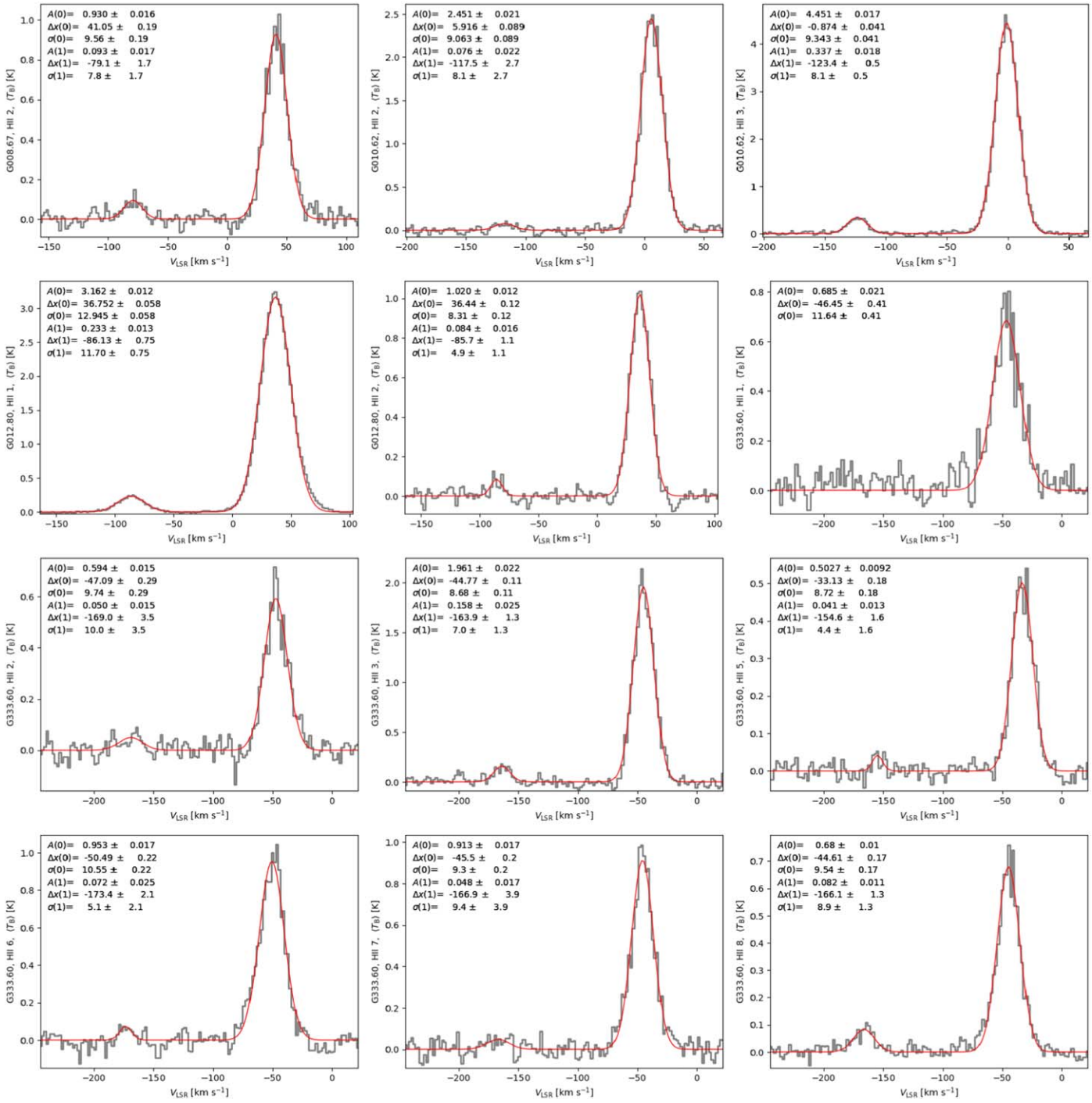

Figure 11. Fits to H41α ($\nu_0 = 92.034434$ GHz) and He41α ($\nu_0 = 92.071938$ GHz) recombination line emission in the 12 protoclusters with detection. This figure shows the H II regions not shown in Figure 5, from those listed in Table 2. The fitted parameters and derived abundances are listed in Table 3.

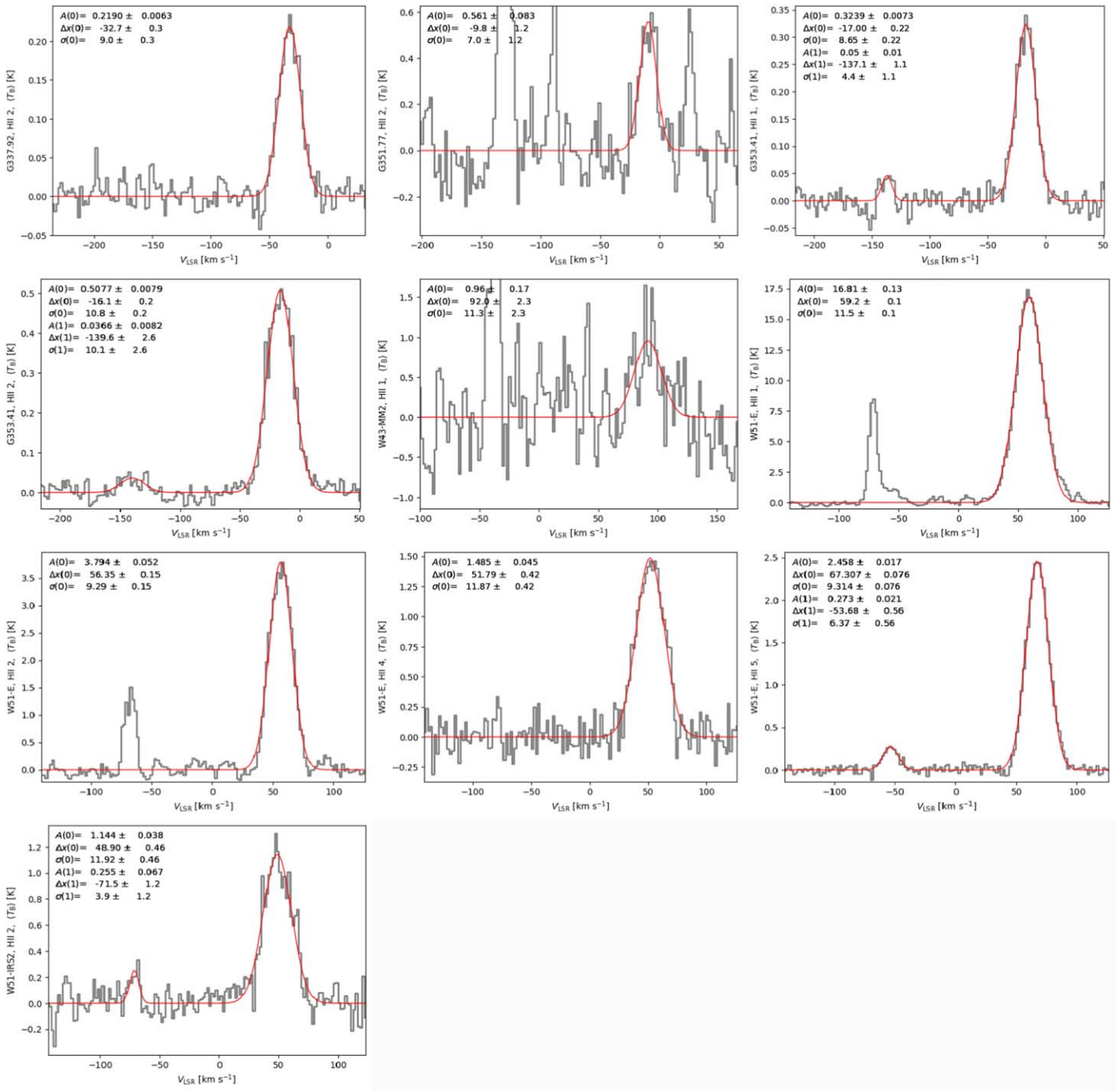

Figure 11. (Continued.)

Appendix D
Abundance and Metallicity Definitions

In most contexts within astronomy, such as in stellar astrophysics and nucleosynthesis, elemental abundances are given in mass units relative to the total mass M as in

$$X + Y + Z = 1, \tag{D1}$$

where X, Y, and Z refer to the hydrogen, helium, and "metals," respectively.

Therefore, the relative mass abundance of helium is given by

$$Y = 1 - Z - \frac{m_{\rm H} N_{\rm H}}{M}, \tag{D2}$$

where $m_{\rm H}$ is the mass of atomic hydrogen, $N_{\rm H}$ is the total number of hydrogen atoms.

Rearranging in terms of observables we have

$$Y = (1 - Z)\left(1 - \frac{1}{1 + (N_{\rm He}/N_{\rm H})(m_{\rm He}/m_{\rm H})}\right), \tag{D3}$$

where the atomic He-to-H mass ratio is $4.002062/1.00784 = 3.97147$.

The solar metallicity is often quoted as $Z_\odot = 0.02$, but recent revisions have taken the value down to $Z_\odot = 0.0153$ (Caffau et al. 2011), a value which is used in modern stellar models (e.g., Bressan et al. 2012). Excluding the low- and high-outliers

G353.41 and W43-MM2, our typical measured values for N_{He}/N_H in the ALMA-IMF H II regions are in the range from 0.065 to 0.104, with typical errors of ± 0.005. Using $Z_\odot$ from Caffau et al. (2011), this translates into $Y = 0.202 \pm 0.012$ to $Y = 0.288 \pm 0.010$. These values are consistent with the inferred values $Z_\odot/X_\odot = 0.0209$, $Y_\odot = 0.2526$ by Caffau et al. (2011). Increasing $Z_\odot$ to 0.02 decreases the inferred values of Y by ~ 0.001.

ORCID iDs

Roberto Galván-Madrid https://orcid.org/0000-0003-1480-4643
Daniel J. Díaz-González https://orcid.org/0000-0002-6325-8717
Frédérique Motte https://orcid.org/0000-0003-1649-8002
Adam Ginsburg https://orcid.org/0000-0001-6431-9633
Nichol Cunningham https://orcid.org/0000-0003-3152-8564
Karl M. Menten https://orcid.org/0000-0001-6459-0669
Fabien Louvet https://orcid.org/0000-0003-3814-4424
Rudy Rivera-Soto https://orcid.org/0000-0002-2162-8441
Patricio Sanhueza https://orcid.org/0000-0002-7125-7685
Amelia M. Stutz https://orcid.org/0000-0003-2300-8200
Tapas Baug https://orcid.org/0000-0003-0295-6586
Hong-Li Liu https://orcid.org/0000-0003-3343-9645

References

Anderson, L. D., Luisi, M., Liu, B., et al. 2021, ApJS, 254, 28
Armante, M., Gusdorf, A., Louvet, F., et al. 2024, A&A, 686, A122
Arthur, S. J., & Hoare, M. G. 2006, ApJS, 165, 283
Astropy Collaboration, Robitaille, T. P., Tollerud, E. J., et al. 2013, A&A, 558, A33
Astropy Collaboration, Price-Whelan, A. M., Sipőcz, B. M., et al. 2018, AJ, 156, 123
Bisbas, T. G., Haworth, T. J., Williams, R. J. R., et al. 2015, MNRAS, 453, 1324
Bonfand, M., Csengeri, T., Bontemps, S., et al. 2024, A&A, 687, A163
Bressan, A., Marigo, P., Girardi, L., et al. 2012, MNRAS, 427, 127
Brouillet, N., Despois, D., Molet, J., et al. 2022, A&A, 665, A140
Caffau, E., Ludwig, H. G., Steffen, M., Freytag, B., & Bonifacio, P. 2011, SoPh, 268, 255
Carrasco-González, C., Galván-Madrid, R., Anglada, G., et al. 2012, ApJL, 752, L29
CASA Team, Bean, B., Bhatnagar, B., et al. 2022, PASP, 134, 114501
Churchwell, E. 2002, ARA&A, 40, 27
Crowther, P. A. 2007, ARA&A, 45, 177
Csengeri, T., Bontemps, S., Wyrowski, F., et al. 2017, A&A, 601, A60
Csengeri, T., Urquhart, J. S., Schuller, F., et al. 2014, A&A, 565, A75
Cunningham, N., Ginsburg, A., Galván-Madrid, R., et al. 2023, A&A, 678, A194
De Pree, C. G., Mehringer, D. M., & Goss, W. M. 1997, ApJ, 482, 307
De Pree, C. G., Wilner, D. J., Mercer, A. J., et al. 2004, ApJ, 600, 286
De Pree, C. G., Peters, T., Mac Low, M. M., et al. 2014, ApJL, 781, L36
Díaz-González, D. J., Galván-Madrid, R., Ginsburg, A., et al. 2023, ApJS, 269, 55
Galván-Madrid, R., Goddi, C., & Rodríguez, L. F. 2012, A&A, 547, L3
Galván-Madrid, R., Keto, E., Zhang, Q., et al. 2009, ApJ, 706, 1036
Galván-Madrid, R., Zhang, Q., Izquierdo, A., et al. 2023, ApJL, 942, L7
Garay, G., & Lizano, S. 1999, PASP, 111, 1049
Ginsburg, A., Sokolov, V., de Val-Borro, M., et al. 2022a, AJ, 163, 291
Ginsburg, A., Goss, W. M., Goddi, C., et al. 2016, A&A, 595, A27
Ginsburg, A., Goddi, C., Kruijssen, J. M. D., et al. 2017, ApJ, 842, 92
Ginsburg, A., Csengeri, T., Galván-Madrid, R., et al. 2022b, A&A, 662, A9
Goddi, C., Ginsburg, A., & Zhang, Q. 2016, A&A, 589, A44
Gordon, M. A., & Sorochenko, R. L. 2002, Radio Recombination Lines. Their Physics and Astronomical Applications (Dordrecht: Kluwer)
Guzmán, A. E., Sanhueza, P., Zapata, L., Garay, G., & Rodríguez, L. F. 2020, ApJ, 904, 77
Hoare, M. G., Kurtz, S. E., Lizano, S., Keto, E., & Hofner, P. 2007, in Protostars and Planets V, ed. B. Reipurth, D. Jewitt, & K. Keil (Tucson, AZ: Univ. Arizona Press), 181
Jiménez-Serra, I., Báez-Rubio, A., Martín-Pintado, J., Zhang, Q., & Rivilla, V. M. 2020, ApJL, 897, L33
Jorsater, S., & van Moorsel, G. A. 1995, AJ, 110, 2037
Keto, E. 2002, ApJ, 580, 980
Keto, E., & Wood, K. 2006, ApJ, 637, 850
Keto, E., Zhang, Q., & Kurtz, S. 2008, ApJ, 672, 423
Kim, K.-T., & Koo, B.-C. 2001, ApJ, 549, 979
Kim, W. J., Urquhart, J. S., Wyrowski, F., Menten, K. M., & Csengeri, T. 2018, A&A, 616, A107
Kim, W. J., Wyrowski, F., Urquhart, J. S., Menten, K. M., & Csengeri, T. 2017, A&A, 602, A37
Klaassen, P. D., Johnston, K. G., Urquhart, J. S., et al. 2018, A&A, 611, A99
Kurtz, S. 2005, in IAU Symp. 227, Massive Star Birth: A Crossroads of Astrophysics, ed. R. Cesaroni et al. (Cambridge: Cambridge Univ. Press), 111
Kurtz, S., Churchwell, E., & Wood, D. O. S. 1994, ApJS, 91, 659
Law, C. J., Zhang, Q., Öberg, K. I., et al. 2021, ApJ, 909, 214
Liu, H. B., Chen, H.-R. V., Román-Zúñiga, C. G., et al. 2019, ApJ, 871, 185
Louvet, F., Sanhueza, P., Stutz, A., et al. 2024, arXiv:2407.18719
Martins, F., Schaerer, D., & Hillier, D. J. 2005, A&A, 436, 1049
Méndez-Delgado, J. E., Esteban, C., García-Rojas, J., Arellano-Córdova, K. Z., & Valerdi, M. 2020, MNRAS, 496, 2726
Meng, F., Sánchez-Monge, Á., Schilke, P., et al. 2022, A&A, 666, A31
Motte, F., Schilke, P., & Lis, D. C. 2003, ApJ, 582, 277
Motte, F., Nony, T., Louvet, F., et al. 2018, NatAs, 2, 478
Motte, F., Bontemps, S., Csengeri, T., et al. 2022, A&A, 662, A8
Nguyen-Luong, Q., Anderson, L. D., Motte, F., et al. 2017, ApJL, 844, L25
Nony, T., Galván-Madrid, R., Motte, F., et al. 2023, A&A, 674, A75
Nony, T., Galván-Madrid, R., Brouillet, N., et al. 2024, A&A, 687, A84
Osterbrock, D. E. 1989, Astrophysics of Gaseous Nebulae and Active Galactic Nuclei (Mill Valley, CA: Univ. Science Books)
Panagia, N. 1973, AJ, 78, 929
Peters, T., Banerjee, R., Klessen, R. S., et al. 2010a, ApJ, 711, 1017
Peters, T., Longmore, S. N., & Dullemond, C. P. 2012, MNRAS, 425, 2352
Peters, T., Mac Low, M.-M., Banerjee, R., Klessen, R. S., & Dullemond, C. P. 2010b, ApJ, 719, 831
Pouteau, Y., Motte, F., Nony, T., et al. 2022, A&A, 664, A26
Pouteau, Y., Motte, F., Nony, T., et al. 2023, A&A, 674, A76
Purcell, C. R., Hoare, M. G., Cotton, W. D., et al. 2013, ApJS, 205, 1
Rivera-Soto, R., Galván-Madrid, R., Ginsburg, A., & Kurtz, S. 2020, ApJ, 899, 94
Robitaille, T., & Bressert, E., 2012 APLpy: Astronomical Plotting Library in Python, Astrophysics Source Code Library, ascl:1208.017
Roelfsema, P. R., & Goss, W. M. 1992, A&ARv, 4, 161
Rosero, V., Hofner, P., Kurtz, S., et al. 2019, ApJ, 880, 99
Roshi, D. A., Balser, D. S., Bania, T. M., Goss, W. M., & De Pree, C. G. 2005, ApJ, 625, 181
Rota, A. A., Meijerhof, J. D., van der Marel, N., et al. 2024, A&A, 684, A134
Rugel, M. R., Rahner, D., Beuther, H., et al. 2019, A&A, 622, A48
Sandell, G., Goss, W. M., Wright, M., & Corder, S. 2009, ApJL, 699, L31
Schuller, F., Menten, K. M., Contreras, Y., et al. 2009, A&A, 504, 415
Shi, H., Zhao, J.-H., & Han, J. L. 2010, ApJ, 710, 843
Spitzer, L. 1978, Physical Processes in the Interstellar Medium (New York: Wiley)
van der Tak, F. F. S., & Menten, K. M. 2005, A&A, 437, 947
Walmsley, C. M. 1990, A&AS, 82, 201
Wenger, T. V., Balser, D. S., Anderson, L. D., & Bania, T. M. 2019, ApJ, 887, 114
Wilson, T. L., Rohlfs, K., & Hüttemeister, S. 2009, Tools of Radio Astronomy (Berlin: Springer)
Wood, D. O. S., & Churchwell, E. 1989, ApJS, 69, 831
Wyrowski, F., Schilke, P., Hofner, P., & Walmsley, C. M. 1997, ApJL, 487, L171
Yang, A. Y., Urquhart, J. S., Thompson, M. A., et al. 2021, A&A, 645, A110
Zamora-Avilés, M., Vázquez-Semadeni, E., González, R. F., et al. 2019, MNRAS, 487, 2200
Zhang, Q., Ho, P. T. P., & Ohashi, N. 1998, ApJ, 494, 636
Zhang, Y., Tanaka, K. E. I., Tan, J. C., et al. 2022, ApJ, 936, 68
Zhu, F. Y., Wang, J. Z., Zhu, Q. F., & Zhang, J. S. 2022, A&A, 665, A94